Research Article

Nikhil M. Kulkarni and Achchhe Lal*

Effect of random variation in input parameter on cracked orthotropic plate using extended isogeometric analysis (XIGA) under thermomechanical loading

Abstract: This research introduces the Stochastic Extended Isogeometric Analysis (XIGA) method to investigate fracture behavior of isotropic and orthotropic materials under mechanical, thermal, and thermomechanical loads. Employing knot spans from Isogeometric Analysis (IGA) for domain discretization, the study utilizes identical basis functions for geometry construction and solution discretization. Utilizing Extended Finite Element Method (XFEM) enrichment functions, accurate crack face displacement discontinuity and tip singularity within the stress field are characterized. Additionally, employing a second-order perturbation technique within XIGA framework, the research derives mean and coefficient of variance values for mixed-mode Stress Intensity Factors (SIF). Stochastic variations in material elastic properties, crack length, and crack angle are considered in this computation. Credibility and robustness of the study are confirmed through comparative analyses against available literatures and Monte Carlo Simulations (MCS). The observed exceptional agreement validates the precision and reliability of the proposed stochastic XIGA method for fracture analysis in orthotropic material systems under thermomechanical loading conditions.

Keywords: Extended isogeometric analysis XIGA, orthotropic cracked plate, stochastic fracture analysis, stress intensity factors, thermo-mechanical loading

* **Corresponding author: Achchhe Lal,** Department of Mechanical Engineering, S. V. National Institute of Technology, Surat, 395007, Gujarat, India, e-mail: achchhelal@med.svnit.ac.in
Nikhil M. Kulkarni: Department of Mechanical Engineering, S. V. National Institute of Technology, Surat, 395007, Gujarat, India; Parul Institute of Engineering and Technology, Faculty of Engineering and Technology, Parul University, Vadodara, 391760, Gujarat, India, e-mail: nikmkul@gmail.com

1 Introduction

Orthotropic composite materials have gained widespread recognition in various industries due to their remarkable properties, including their high strength, adaptability in design, favorable stiffness-to-weight ratios, and impressive resistance to corrosion and fatigue. These materials have found extensive applications across multiple sectors such as aerospace, spacecraft, marine, automotive, civil engineering, and the medical field. Despite their numerous advantages, the intricate manufacturing procedures involved in creating orthotropic composites often result in flaws like internal and external cracks, voids, inclusions, and porosities. These flaws significantly increase stress concentrations near their location or close to crack tips, consequently reducing the overall strength and fracture toughness of the structures.

Precisely calculating fracture parameters, particularly Mixed Mode Stress Intensity Factors (MMSIFs), holds paramount importance in improving the resilience of cracked structures against crack propagation. When structures experience different loadings, like in-plane or out-of-plane stresses along with thermal stresses thereof, accurately evaluating MMSIFs becomes crucial to guarantee dependable fracture characteristics. This precise assessment is vital for ensuring the reliability of fracture behavior in these structures.

XIGA seamlessly integrates CAD and analysis, making it easier to handle complex geometries and interfaces without the need for extensive meshing processes. The use of NURBS (Non-Uniform Rational B-Splines) allows for precise representation of complex shapes and smooth surfaces. Traditional FEM requires body-fitted meshes that conform to the geometry, which can be time-consuming and challenging to generate for complex multi-material interfaces. XIGA, however, can handle non-conforming meshes, reducing the meshing effort and improving the efficiency of the modeling process. XIGA can naturally represent discontinuities (such as cracks or material interfaces) by enriching

the solution space with additional functions (like Heaviside functions or crack tip enrichment functions). This capability is particularly useful in multi-material problems where discontinuities are prevalent. NURBS basis function opted in XIGA provides higher-order continuity, which enhances the accuracy of representing gradients and discontinuities in the physical response of the materials when compared to traditional XFEM. XIGA can also directly use CAD models for analysis without the need for intermediate meshing steps, streamlining the workflow and reducing potential sources of error.

In summary, XIGA stands out in handling intricate geometries, capturing discontinuities, and managing large spatial gradients. It enhances accuracy and convergence while lowering computational costs, making it an excellent choice for multi-material problems compared to traditional FEM, XFEM, or other methods.

In the journey from manufacturing through processing to practical utilization, structures created from orthotropic materials exhibit notable variability owing to different factors. These encompass material properties, intricate geometries, crack specifications, and external loads. This distinctiveness sets them apart from conventional isotropic materials during manufacturing processes. The absence of comprehensive control at each design phase leads to dispersion in system properties. As these system parameters fluctuate randomly, the resulting variability extends to MMSIFs (Mixed Mode Stress Intensity Factors). Consequently, the statistical behavior of MMSIFs may vary depending on their sensitivity to input random variables and their distribution patterns.

Therefore, it becomes crucial to precisely quantify this variability at various levels to align the statistical representation of MMSIFs closely with their actual values. This alignment is fundamental to ensuring that structures maintain an appropriate safety margin and reliability. Such considerations underscore the necessity for a more refined probabilistic approach when analyzing these intricate cracked orthotropic materials.

Probabilistic methodologies, such as Monte Carlo simulations (MCS) rooted in statistics, and non-statistical perturbation methods, have seen increased adoption for assessing response statistics. Perturbation techniques, in particular, are favored for examining structures influenced by system randomness. While Monte Carlo simulations serve as an ideal tool for validating proposed techniques, they often entail higher computational expenses compared to perturbation methods.

It's fascinating how fracture mechanics faces challenges in practical scenarios due to intricate features like arbitrary geometries, nonlinear material behavior, and complex loadings. These factors often constrain the effectiveness of traditional analytical methods [1–3]. Consequently, researchers are pivoting towards advanced numerical techniques, including boundary element methods, finite element methods, meshless approaches, and extended finite element methods. These innovative methods offer more comprehensive solutions to tackle these complexities in fracture mechanics.

XFEM stands as a significant advancement in fracture mechanics, enabling the representation of cracks without alignment to element edges. This innovation includes incorporating enrichment functionalities, obtained by asymptotic analytical solution, into conventional FE shape functions. By doing so, these enriched functions possess the capability to faithfully replicate crack face discontinuities & intricate stress patterns near the tip of the crack. Notably, XFEM eliminates the requirement for singular elements or remeshing during crack propagation, providing a more efficient and accurate approach to analyzing crack behavior within structures [4–6].

In the realm of fracture analysis concerning composite materials, specialized enrichment functions designed for these applications have been introduced. These encompass static orthotropic functions [7,8] dynamic orthotropic solutions [9,10] and specific considerations for anisotropic bi-material delamination [11]. These tailored enrichment functions cater to the nuanced complexities observed in composite materials, providing more precise and detailed analyses for fracture behavior within these structures.

Hughes indeed presented Isogeometric Analysis (IGA) as a substitute for the FEM, harnessing Non-Uniform Rational B-spline (NURBS) technology, which is frequently employed in computer graphics. In IGA, NURBS functions play a dual role: not only do they precisely define the geometry, but they also serve in approximating the solutions. This dual functionality of NURBS in IGA is pivotal, as it allows for more seamless integration between geometric design and analysis, offering advantages in accuracy and efficiency in numerical simulations and modeling [12].

IGA has showcased significant success across diverse engineering domains. Its applications extend to areas like shape optimization [13,14], shell analysis [15,16], analysis of FGM, and the study of laminated composite plates [17,18]. The inherent advantages of IGA, especially its seamless integration of geometric modeling using NURBS and numerical analysis, have proven particularly beneficial in these domains, enabling more accurate and efficient simulations and analyses in complex engineering scenarios.

IGA scope is expanded to tackle issues related to fractures using a method known as extended isogeometric analysis (XIGA) [19,20]. This modification integrates XFEM enrichment technique into IGA, enabling the representation of irregularities in crack surfaces and the precise depiction of stress concentrations around crack tips. To extend the scope,

the XIGA method outlined in [19] has undergone further development. This advancement involves the inclusion of FGM composites and the consideration of thermomechanical loadings in different materials. Multiple researchers have delved into the study of cracked FGM through various methods: experimental approaches [21] as well as numerical and analytical techniques [22–27].

The exploration of stochastic fracture behavior in isotropic and orthotropic plates under varied loading conditions remains a relatively limited area of research globally. Chopra *et al.* [28] contributed significantly by initiating the formulation for single-edge notched panel with multiple fractures probabilistic analysis. Their study employed the finite element method within a framework of random loadings, examining symmetric and asymmetric fracture configurations, and established connections between their findings and empirical observations.

Investigation of the applicability of J-estimation models in the probabilistic analysis of elastic-plastic behavior in structures with cracks. Rahman offered numerical instances demonstrating probabilistic analysis. These instances accounted for uncertainties of loads, crack dimensions, and material properties within two- and three-dimensional cracked structures [29]. Furthermore, expansion to Rahman's model is to evaluate the fracture behavior in ductile cracked structures. Their approach combined conventional FEM with reliability techniques like FORM, SORM, and Monte Carlo simulations to assess the reliability and probabilistic fracture response of diverse structures [30].

Experiments are performed to explore the probabilistic characteristics of edge-delamination strength in thermosetting polymer composites. Their experimental approach involved the utilization of acoustic emission apparatus, as well as optical and scanning electron microscopes, enabling the observation of edge-delamination inception, failure modes, and the establishment of probabilistic models [31].

A stochastic micro-mechanical model is presented employing a refined two-dimensional triangular spring network. These models aimed at investigating fracture behavior within randomly structured fiber-matrix composites. The focus was on comprehending the influence of geometric variability on crack propagation paths within these composite materials [32].

Introducing the scaled boundary finite element method (SBFEM) for analyzing how uncertainties in crack geometry influence the reliability of cracked structures. They performed reliability evaluations employing Monte Carlo simulations (MCS) [33].

A novel method known as the moment-modified polynomial dimensional decomposition technique is utilized to analyze 3-D FGM for stochastic multiscale fractures, allowing for arbitrary boundary conditions [34]. Meanwhile, a swift reliability analysis technique was introduced for composite grillages by integrating the Navier grillage method into the finite element framework [35].

A stochastic multiscale approach aimed at examining the impact of correlated input parameters on characteristics of composites. Their technique involved hierarchical multiscale modeling and sensitivity analysis techniques [36]. Additionally, Lal *et al.* [37] as well as Lal and Palekar [38] evaluated statistical properties associated with Mode I SIF in single-edge notched laminated composite plates. They utilized displacement correlation methods in conjunction with second-order perturbation techniques (SOPT) and Monte Carlo simulations (MCS) for their assessments.

XFEM is employed for analyzing the fracture behavior of FGM under both thermomechanical and mechanical loadings [39,40]. Additionally, numerous researchers have utilized numerical methods such as finite and boundary elements to investigate the fracture of cracked solids under thermal loading [41–44].

In addition to conventional Lagrange polynomial discretizations, some numerical examples are presented, which demonstrate that the formulation based on IGA offers a computationally accurate and efficient solution for challenging interface debonding problems in both 2D and 3D [45].

This study applies a strong formulation finite element method, along with its localized version and the isogeometric approach, to classic examples like plane stress plates with circular holes, U-shaped holes, and V-notches. The numerical results closely match the reference results, demonstrating the potential and accuracy of these methods in capturing stress concentrations in fracture mechanics, even with coarse mesh discretizations [46].

In this article, the level set method is combined with the extended finite element method (XFEM) to forecast the direction of fracture propagation in a specimen and to calculate the stress intensity factor for cracked plates under various loading scenarios [47].

In this study, the extended finite element method (XFEM) is employed to model a semi-circular bending test, focusing on the initiation and propagation of cracks in rock. Special attention is given to the effects of notch size and scale on the fracturing behavior of the specimen, particularly concerning peak load [48].

The current body of literature offers limited exploration into the impact of thermomechanical loads on cracked orthotropic materials. Few studies delve into stochastic fracture analysis of orthotropic plates with use FEM & XFEM. Moreover, there is a scarcity of research employing XIGA to account for thermomechanical load effects.

In this article, we assess the Mixed-Mode Stress Intensity Factor (SIF) in orthotropic plates containing through-

thickness cracks subjected to thermomechanical loadings. In this article, an assessment of Mixed-Mode SIF in orthotropic plates with through-thickness cracks is done under thermomechanical loadings. It aims to explore the mean and coefficient of variance of normalized MMSIFs while changing parameters such as crack length, temperature, and elastic material properties. Employing the stochastic XIGA method along with second-order perturbation techniques (SOPT) and Monte Carlo simulations (MCS), this research aims to evaluate the mean and COV properties of MMSIFs.

2 Formulation

2.1 Fracture analysis

The orthotropic structure with a crack is defined within global cartesian coordinates (X, Y), aligning its elastic symmetry axes with local Cartesian axes (x_1, y_1). The crack tip is represented using local polar coordinates (r, θ). as illustrated in Figure 1.

The body encounters various forces alongside different displacement and traction boundary conditions. Expressing orthotropic stress–strain relationship by:

$$\sigma_i = C_{ij}\varepsilon_j. \tag{1}$$

The relevant compliance coefficients of body are C_{ij} $(i, j = 1, 2, 6)$ in local Cartesian coordinates. The stress–strain equation is given as [49]

Figure 1: Cracked orthotropic body experiencing traction forces. This area is enclosed by the contour r and contains arbitrary boundary conditions within the designated area A.

$$\sigma_{x_1} = C_{11}\frac{\partial u_{x_1}}{\partial x_1} + C_{12}\frac{\partial v_{y_1}}{\partial y_1}, \tag{2}$$

$$\sigma_{y_1} = C_{12}\frac{\partial u_{x_1}}{\partial x_1} + C_{22}\frac{\partial v_{y_1}}{\partial y_1}, \tag{3}$$

$$\tau_{x_1y_1} = C_{66}\left(\frac{\partial u_{x_1}}{\partial x_1} + \frac{\partial v_{y_1}}{\partial y_1}\right). \tag{4}$$

Further, in-plane elastostatic set of equations is given as follows:

$$\frac{\partial^2 u}{\partial x_1^2} + \left(\frac{C_{66}}{C_{11}}\right)\frac{\partial^2 u}{\partial y_1^2} + 2\left(\frac{C_{12} + C_{66}}{2C_{11}}\right)\frac{\partial^2 v}{\partial x_1\partial y_1} = 0, \tag{5}$$

$$\frac{\partial^2 v}{\partial x_1^2} + \left(\frac{C_{22}}{C_{66}}\right)\frac{\partial^2 v}{\partial y_1^2} + 2\left(\frac{C_{12} + C_{66}}{2C_{66}}\right)\frac{\partial^2 u}{\partial x_1\partial y_1} = 0. \tag{6}$$

The partial differential equation governing the fourth order for an orthotropic body, derived from compatibility and equilibrium considerations, can be stated as follows: [37,38]

$$C_{11}\mu^4 - 2C_{16}\mu^3 + (2C_{12} + C_{66})\mu^2 - 2C_{26}\mu + C_{22} = 0. \tag{7}$$

Complex or purely imaginary roots of Eq. (7) and are derived as $(\mu_k = \mu_{kx_1} + i\mu_{ky_1})$ which always occur in conjugate pairs as μ_1, $\overline{\mu_1}$ and μ_2, $\overline{\mu_2}$.

Complex variables and analytical functions $(z_k = x_1 + \mu_k y_{1k}$ $(k = 1, 2))$ are employed to delineate the two-dimensional displacement and stress fields surrounding the crack tip [50] The pure mode I stress components given by,

$$\sigma_{11}^{\mathrm{I}} = \frac{K_{\mathrm{I}}}{(2\pi r)^{1/2}}$$
$$\times \mathrm{Re}\left[\frac{\mu_1\mu_2}{\mu_1 - \mu_2}\left(\frac{\mu_2}{(\cos\theta + \mu_2\sin\theta)^{1/2}} - \frac{\mu_1}{(\cos\theta + \mu_1\sin\theta)^{1/2}}\right)\right], \tag{8}$$

$$\sigma_{22}^{\mathrm{I}} = \frac{K_{\mathrm{I}}}{(2\pi r)^{1/2}}$$
$$\times \mathrm{Re}\left[\frac{1}{\mu_1 - \mu_2}\left(\frac{\mu_1}{(\cos\theta + \mu_2\sin\theta)^{1/2}} - \frac{\mu_2}{(\cos\theta + \mu_1\sin\theta)^{1/2}}\right)\right], \tag{9}$$

$$\tau_{12}^{\mathrm{I}} = \frac{K_{\mathrm{I}}}{(2\pi r)^{1/2}}$$
$$\times \mathrm{Re}\left[\frac{\mu_1\mu_2}{\mu_1 - \mu_2}\left(\frac{1}{(\cos\theta + \mu_1\sin\theta)^{1/2}} - \frac{1}{(\cos\theta + \mu_2\sin\theta)^{1/2}}\right)\right], \tag{10}$$

and the corresponding displacements are given as

$$
u^{\text{I}} = K_{\text{I}}\left(\frac{2r}{\pi}\right)^{1/2}
$$
$$
\times \operatorname{Re}\left\{\frac{1}{\mu_1 - \mu_2}\left[\begin{matrix}\mu_1 p_2(\cos\theta + \mu_2\sin\theta)^{1/2} - \\ \mu_2 p_1(\cos\theta + \mu_1\sin\theta)^{1/2}\end{matrix}\right]\right\}, \tag{11}
$$

$$
v^{\text{I}} = K_{\text{I}}\left(\frac{2r}{\pi}\right)
$$
$$
\times \operatorname{Re}\left\{\frac{1}{\mu_1 - \mu_2}\left[\begin{matrix}\mu_1 q_2(\cos\theta + \mu_2\sin\theta)^{1/2} - \\ \mu_2 q_1(\cos\theta + \mu_1\sin\theta)^{1/2}\end{matrix}\right]\right\}, \tag{12}
$$

$$
w^{\text{I}} = 0. \tag{13}
$$

Pure mode II stress and displacement are:

$$
\sigma_{11}^{\text{II}} = \frac{K_{\text{II}}}{(2\pi r)^{1/2}}
$$
$$
\times \operatorname{Re}\left[\frac{1}{\mu_1 - \mu_2}\left(\begin{matrix}\dfrac{\mu_2^2}{(\cos\theta + \mu_2\sin\theta)^{1/2}} - \\ \dfrac{\mu_1^2}{(\cos\theta + \mu_1\sin\theta)^{1/2}}\end{matrix}\right)\right], \tag{14}
$$

$$
\sigma_{22}^{\text{II}} = \frac{K_{\text{II}}}{(2\pi r)^{1/2}}
$$
$$
\times \operatorname{Re}\left[\frac{1}{\mu_1 - \mu_2}\left(\begin{matrix}\dfrac{1}{(\cos\theta + \mu_2\sin\theta)^{1/2}} - \\ \dfrac{1}{(\cos\theta + \mu_1\sin\theta)^{1/2}}\end{matrix}\right)\right], \tag{15}
$$

$$
\tau_{12}^{\text{II}} = \frac{K_{\text{II}}}{(2\pi r)^{1/2}}
$$
$$
\times \operatorname{Re}\left[\frac{1}{\mu_1 - \mu_2}\left(\begin{matrix}\dfrac{\mu_1}{(\cos\theta + \mu_1\sin\theta)^{1/2}} - \\ \dfrac{\mu_2}{(\cos\theta + \mu_2\sin\theta)^{1/2}}\end{matrix}\right)\right], \tag{16}
$$

and the displacement is given as

$$
u^{\text{II}} = K_{\text{II}}\left(\frac{2r}{\pi}\right)^{1/2}
$$
$$
\times \operatorname{Re}\left\{\frac{1}{\mu_1 - \mu_2}\left[\begin{matrix}p_2(\cos\theta + \mu_2\sin\theta)^{1/2} - \\ p_1(\cos\theta + \mu_1\sin\theta)^{1/2}\end{matrix}\right]\right\}, \tag{17}
$$

$$
v^{\text{II}} = K_{\text{II}}\left(\frac{2r}{\pi}\right)^{1/2}
$$
$$
\times \operatorname{Re}\left\{\frac{1}{\mu_1 - \mu_2}\left[\begin{matrix}q_2(\cos\theta + \mu_2\sin\theta)^{1/2} - \\ q_1(\cos\theta + \mu_1\sin\theta)^{1/2}\end{matrix}\right]\right\}, \tag{18}
$$

$$
w^{\text{II}} = 0. \tag{19}
$$

In this scenario, K_{I} denotes the mode I stress intensity factors (SIF), and K_{II} denotes the mode II stress intensity factors (SIF). "Re" indicates the real part of the statement, while p_k and q_k are further explained below.

$$
p_k = C_{11}\mu_k^2 + C_{12} - C_{16}\mu_k, \tag{20}
$$

$$
q_k = C_{12}\mu_k + \frac{C_{22}}{\mu_k} - C_{26}. \tag{21}
$$

2.2 XIGA formulation

To effectively address problems involving discontinuities such as cracks, integrating concepts from XFEM with IGA significantly enhances their capabilities. XFEM is adept at handling static and dynamic discontinuities within structures, while IGA demonstrates precision and efficiency in analyzing complex geometries. Merging these methodologies, known as XIGA, allows for defining the entire crack independently of the mesh. XIGA essentially represents IGA approximation enriched by the application of partition of unity (PU), which is derived from the XFEM formulation.

To model singular fields and discontinuities, XIGA improves the local isogeometric approximation by introducing extra degrees of freedom at certain points near crack locations within the basic IGA model. Enrichment functions are used to contribute to overall approximation. In the XIGA method, crack-tip enrichment functions are utilized for capturing singularity within the stress fields at the crack tip, whereas Heaviside functions are employed for the representation of the crack face (Figure 2).

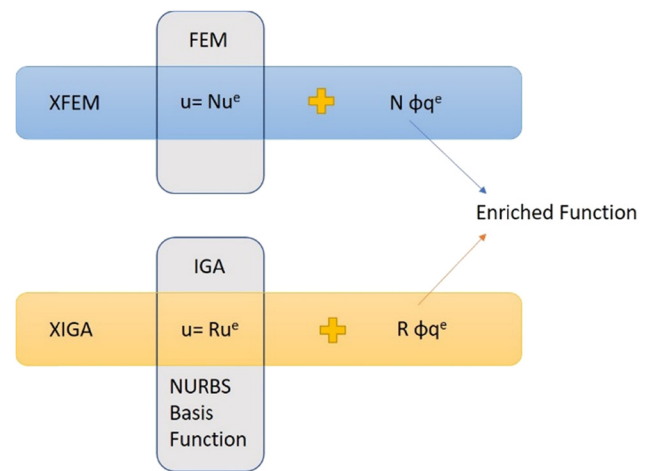The generalized expression for the displacement approximation at the designated control point corresponding to ξ_i is:

Figure 2: Sketch depicting the arrangement of various methods.

$$\begin{aligned}
\mathbf{u}^{\mathrm{h}}(\xi) = {} & \sum_{i=1}^{n_{\mathrm{en}}} R_i(\xi)\mathbf{u}_i \\
& + \left\{ \sum_{j=1}^{n_{\mathrm{cf}}} R_j(\xi)[H(\xi) - H(\xi_i)]\mathbf{a}_j \right\} B_{\mathrm{H}} \\
& + \left\{ \sum_{k=1}^{n_{\mathrm{ct}}} R_k(\xi) \left\{ \sum_{a=1}^{4} [\beta_a(\xi) - \beta_a(\xi_i)]\mathbf{b}_k^a \right\} \right\} B_{\mathrm{T}} \\
& + \sum_{i=1}^{n_{\mathrm{h}}} R_j(\xi)[\chi(\xi) - \chi(\xi_i)]\mathbf{c}_j \\
& + \sum_{i=1}^{n_{\mathrm{in}}} R_j(\xi)\psi(\xi)\mathbf{d}_j,
\end{aligned} \tag{22}$$

where u_i signifies parameters related to the particular control point; n_{en} refers to the number of basis functions for each element; R_i^p denotes the rational B-spline basis functions; n_{cf} denotes the number of basis functions entirely intersected by the crack face; n_{ct} represents the number of basis functions partially intersected by the crack tip; n_{h} is the count of basis functions partially intersected by the hole; and n_{in} indicates the number of basis functions partially intersected by the inclusion.

Additional control points influence enriched degrees of freedom as follows:
- a_j accounts for the Heaviside function $H(\xi)$;
- b_k^a influences degrees of freedom associated with asymptotic crack-tip enrichment functions β_a;
- c_j and d_j contribute to control points associated with specific functions, namely $\chi(\xi)$ and $\psi(\xi)$ respectively, characterizing material interfaces.

Blending functions like B_{h} and B_{t} are employed for the Heaviside function and crack-tip function, respectively. The Heaviside function $H(\xi)$ equals +1 when the parametric coordinate ξ corresponds to a particular Gauss point situated above the crack face. Conversely, when ξ lies below the crack face, $H(\xi)$ equals −1.

Strain is comprised of two components in a thermo-mechanical problem.

$$\varepsilon^{\mathrm{t}} = \varepsilon^{\mathrm{m}} + \varepsilon^{\mathrm{th}}, \tag{23}$$

Here, ε^{t} is the total strain, ε^{m} is the mechanical strain, $\varepsilon^{\mathrm{th}}$ is the thermal strain, where $\varepsilon^{\mathrm{th}}$ can be written as for plane stress state,

$$\begin{Bmatrix} \varepsilon_{11}^{\mathrm{th}} \\ \varepsilon_{22}^{\mathrm{th}} \\ \varepsilon_{33}^{\mathrm{th}} \\ 2\varepsilon_{12}^{\mathrm{th}} \end{Bmatrix} = \begin{Bmatrix} \alpha_{11} \\ \alpha_{22} \\ \alpha_{33} \\ 0 \end{Bmatrix} \Delta T, \tag{24}$$

and for plane strain state,

$$\begin{Bmatrix} \varepsilon_{11}^{\mathrm{th}} \\ \varepsilon_{22}^{\mathrm{th}} \\ \varepsilon_{33}^{\mathrm{th}} \\ 2\varepsilon_{12}^{\mathrm{th}} \end{Bmatrix} = \begin{Bmatrix} \mu_{31}\alpha_{33} + \alpha_{11} \\ \mu_{32}\alpha_{33} + \alpha_{22} \\ \alpha_{33} \\ 0 \end{Bmatrix} \Delta T, \tag{25}$$

Thermal expansion coefficient is denoted as α_{ij}, and Poisson's ratio is denoted by μ_{ij}. According to the generalized Hooke's law, the mechanical part of strain, ε^{m} is shown below.

$$\begin{Bmatrix} \varepsilon_{11}^{\mathrm{m}} \\ \varepsilon_{22}^{\mathrm{m}} \\ \varepsilon_{33}^{\mathrm{m}} \\ 2\varepsilon_{23}^{\mathrm{m}} \\ 2\varepsilon_{13}^{\mathrm{m}} \\ 2\varepsilon_{12}^{\mathrm{m}} \end{Bmatrix} = \begin{bmatrix} a_{11} & a_{12} & a_{13} & a_{14} & a_{15} & a_{16} \\ a_{12} & a_{22} & a_{23} & a_{24} & a_{25} & a_{26} \\ a_{13} & a_{23} & a_{33} & a_{34} & a_{35} & a_{36} \\ a_{14} & a_{24} & a_{34} & a_{44} & a_{45} & a_{46} \\ a_{15} & a_{25} & a_{35} & a_{45} & a_{55} & a_{56} \\ a_{16} & a_{26} & a_{36} & a_{46} & a_{56} & a_{66} \end{bmatrix} \begin{Bmatrix} \sigma_{11} \\ \sigma_{22} \\ \sigma_{33} \\ \sigma_{23} \\ \sigma_{13} \\ \sigma_{12} \end{Bmatrix}. \tag{26}$$

The discretized form can be written as

$$K\mathbf{u}^{\mathrm{h}} = f. \tag{27}$$

The displacement vector $\mathbf{u}^{\mathrm{h}}$ encompasses standard as well as additional degrees of freedom.

$$\mathbf{u}^{\mathrm{h}} = \{u \quad a \quad b_1 \quad b_2 \quad b_3 \quad b_4\}. \tag{28}$$

The displacement $\mathbf{u}^{\mathrm{h}}$ represents the standard degrees of freedom, while 'a' and 'ba' (where a ranges from 1 to 4) symbolize additional degrees of freedom utilized for the crack face and fields surrounding the crack tip. The mechanical force vector f and global stiffness matrix K are both assembled from their respective element's contributions.

$$K_{ij}^e = \begin{bmatrix} K_{ij}^{ab} & K_{ij}^{ua} & K_{ij}^{ub} \\ K_{ij}^{au} & K_{ij}^{aa} & K_{ij}^{ab} \\ K_{ij-a}^{bu} & K_{ij}^{ba} & K_{ij}^{bb} \end{bmatrix}, \tag{29}$$

$$f_i = \left\{ f_i^u \quad f_i^a \quad f_i^{b_1} \quad f_i^{b_2} \quad f_i^{b_3} \quad f_i^{b_4} \right\}^{\mathrm{T}}. \tag{30}$$

Similarly, the discretize form of thermal is

$$QT^{\mathrm{h}} + f^{\mathrm{th}} = 0, \tag{31}$$

where T^{h} is the temperature vector

$$T^{\mathrm{h}} = \{u \quad a \quad b_1\}. \tag{32}$$

Thermal force vector f^{th} and thermal stiffness matrix Q are formed using a different matrix of basis function derivatives.

$$Q_{ij}^e = \begin{bmatrix} Q_{ij}^{ab} & Q_{ij}^{ua} & Q_{ij}^{ub} \\ Q_{ij}^{au} & Q_{ij}^{aa} & Q_{ij}^{ab} \\ Q_{ij}^{bu} & Q_{ij}^{ba} & Q_{ij}^{bb} \end{bmatrix}, \tag{33}$$

$$f_i^{\text{th}-e} = \left\{ f_i^{\text{th}-u} \quad f_i^{\text{th}-a} \quad f_i^{\text{th}-h} \right\}, \tag{34}$$

$$f = f^{\text{th-equivalent}} + f^{\text{mech.}}$$
$$= \int B^T C \varepsilon^{\text{th}} \, d\Omega + f^{\text{mech}} . \tag{35}$$

2.2.1 Cracks modeling in extended isogeometric analysis

XIGA merges foundational principles of XFEM enrichments into the framework of IGA. Fields pertaining to displacement, associated with crack faces and crack tips, are incorporated into the conventional IGA approximation in XIGA.

$$\chi = \chi^{\text{IGA}} + \chi^{\text{XIGA}} = \chi^{\text{IGA}} + \chi^{\text{tip}} + \chi^{\text{heaviside}} . \tag{36}$$

Here, χ can be displacement U or temperature T. The $\chi^{\text{heaviside}}$ part of enrichment is utilized for modeling strong discontinuity at the crack face in displacement fields and temperature fields which is given below:

$$\chi^{\text{heaviside}} = \sum_{i \in n_s} N_i(X) H(X) \hat{a}_i, \tag{37}$$

where n_s denotes the collection of control points whose enrichment is done using the Heaviside function. This function, evaluated at a point located at the physical coordinate X, is defined as:

$$H(X) = \begin{cases} +1 \text{ if } (X - X^*) \cdot e_n > 0 \\ -1 \text{ otherwise.} \end{cases} \tag{38}$$

The χ part of the enrichment is used to reproduce the complex analytical crack tip field

$$\chi^{\text{tip}} = \sum_{i \in T_p} N_i(X) \left(\sum_{k \in F} f_k(X) \hat{b}_{ik} \right). \tag{39}$$

In this context, T_p constitutes the collection of control points augmented by the set F of crack tip functions f_k. These functions, originating from the asymptotic solution, possess individual uniqueness tailored to specific problem sets. In the case of the isotropic body subjected to stationary mechanical loads, utilization involves the four distinctive functions given below.

$$F(r, \theta) = \begin{cases} \sqrt{r} \sin\left(\dfrac{\theta}{2}\right), \\ \sqrt{r} \cos\left(\dfrac{\theta}{2}\right), \\ \sqrt{r} \sin(\theta)\sin\left(\dfrac{\theta}{2}\right), \\ \sqrt{r} \sin(\theta)\cos\left(\dfrac{\theta}{2}\right) \end{cases}. \tag{40}$$

The polar coordinates r and θ are measured from the crack tip. Furthermore, for orthotropic materials, a set of four functions has been proposed.

$$F(r, \theta) = \begin{cases} \sqrt{r} \cos\left(\dfrac{\theta_1}{2}\right)\sqrt{g_1(\theta)}, \ \sqrt{r} \sin\left(\dfrac{\theta_1}{2}\right)\sqrt{g_1(\theta)}, \\ \sqrt{r} \cos\left(\dfrac{\theta_2}{2}\right)\sqrt{g_2(\theta)}, \ \sqrt{r} \sin\left(\dfrac{\theta_2}{2}\right)\sqrt{g_2(\theta)} \end{cases}, \tag{41}$$

With

$$g_j(\theta) = \sqrt{(\cos(\theta) + \zeta_j \sin(\theta))^2 + (\beta_j \sin(\theta))^2}, \tag{42}$$

$$\theta_k(\theta) = \tan^{-1}\left(\frac{\beta_k \sin(\theta)}{\cos(\theta) + \zeta_k \sin(\theta)} \right). \tag{43}$$

Roots of characteristic equation consist of both real and complex parts

$$a_{11}^{\text{tip}} \mu^4 - 2a_{16}^{\text{tip}} \mu^3 + (2a_{12}^{\text{tip}} + a_{66}^{\text{tip}})\mu^2 - 2a_{26}^{\text{tip}} \mu + a_{22}^{\text{tip}} = 0, \tag{44}$$

$$\mu_1 = \zeta_1 + i\beta_1, \tag{45}$$

$$\mu_2 = \zeta_2 + i\beta_2, \tag{46}$$

The following tip enrichment is used for the thermal equation:

$$F^{\text{th}}(r, \theta) = \sqrt{r} \sin\left(\frac{\theta}{2}\right). \tag{47}$$

2.2.2 Control points enrichment selection

The approach adopted here is to select enriched control points that mirror the level set method of XFEM, albeit by small variation due to the distinctions between XIGA's control points and XFEM's nodes. In XFEM, only nodes linked to elements containing crack faces or tips undergo enrichment. However, within the XIGA framework, numerous control points, even those distant from the crack, can be

enriched due to broader impact in the domain. The selection criterion involves identifying control points whose respective basis function holds non-zero values at either the crack tip or the crack face. These selected points are enriched using tip enrichment functions or Heaviside functions.

A crucial yet intricate distinction exists in the treatment of control points. The selective utilization originates from acknowledging that augmenting these control points with the Heaviside function inaccurately extends the crack front. By incorporating crack tip enrichments, it becomes possible to precisely replicate the jump across the exact face of the crack. Consequently, control points enriched by these functions maintain the accuracy of the genuine crack's kinematic discontinuity. This capability is intrinsic to crack tip asymptotic function $\sqrt{r}\sin(\theta/2)$ showcasing its effectiveness in reproducing discontinuity at the crack face, whether for isotropic or orthotropic material.

2.2.3 Stress intensity factor (SIF)

Here, we analyzed SIF using the interaction integral method. When dealing with orthotropic problems, three formulations have been proposed: constant constitutive, incompatibility, and non-equilibrium. The non-equilibrium and incompatibility methods tend to yield comparable outcomes, whereas the constant–constitutive way often shows lesser accuracy. In our study, we specifically utilized the incompatibility formulation, which involves calculating the auxiliary strain field.

$$\varepsilon_{kl}^{\text{aux}} = c_{ijkl}^{-1}(x)\sigma_{ij}^{\text{aux}}, \tag{48}$$

$$c_{ijkl}^{-1}(x^{\text{tip}})\sigma_{ij}^{\text{aux}} = \frac{1}{2}(u_{i,j}^{\text{aux}} + u_{j,i}^{\text{aux}}). \tag{49}$$

Below incompatible relations are the result of the discrepancy:

$$\sigma_{ij,j}^{\text{aux}} = 0, \text{ and } \sigma_{ij}^{\text{aux}} = c_{ijkl}(x)\varepsilon_{kl}^{\text{aux}},$$
$$\text{but } \varepsilon_{ij}^{\text{aux}} \neq \frac{1}{2}(u_{i,j}^{\text{aux}} + u_{j,i}^{\text{aux}}). \tag{50}$$

J-integral for a cracked body, where "$^{\text{aux}}$" represents the auxiliary fields, is shown below:

$$J = \int_A (\sigma_{ij}u_{i,1} - w\delta_{1j})q_{,j}\mathrm{d}A$$
$$+ \int_A (\sigma_{ij}u_{i,1} - w\delta_{1j})_j q\mathrm{d}A, \tag{51}$$

where w is the strain energy density and δ_{ij} is the Kronecker delta.

$$w = \frac{1}{2}(\sigma_{11}\varepsilon_{11}^{\text{m}} + \sigma_{22}\varepsilon_{22}^{\text{m}} + 2\sigma_{12}\varepsilon_{12}^{\text{m}}). \tag{52}$$

The article utilizes the interaction integral method, employing the conservation of J integral as an actual and auxiliary state to compute the MMSIF.

$$J = J^{\text{act}} + J^{\text{aux}} + M. \tag{53}$$

In this context, J^{act} and J^{aux} represent the conservation integrals for actual and auxiliary fields, respectively. Comprising both mechanical and thermal terms in a thermo-mechanical scenario, M refers to the interaction integral.

$$M = M^{\text{m}} + M^{\text{th}}, \tag{54}$$

with

$$M^{\text{m}} = \int_A \left\{ \begin{matrix} \sigma_{ij}u_{i,1}^{\text{aux}} + \sigma_{ij}^{\text{aux}}u_{i,1} \\ -\frac{1}{2}(\sigma_{ik}\varepsilon_{ik}^{\text{aux}} + \sigma_{ik}^{\text{aux}}\varepsilon_{ik}^{\text{m}})\delta_{1j} \end{matrix} \right\} q_{,j}\mathrm{d}A$$
$$+ \int_A \{\sigma_{ij}(s_{ijkl}^{\text{tip}} - s_{ijkl}(x))\sigma_{kl,1}^{\text{aux}}\}q\mathrm{d}A, \tag{55}$$

$$M^{\text{th}} = \int_A \{\sigma_{ij}^{\text{aux}}\varepsilon_{ij,1}^{\text{th}}\}q\mathrm{d}A$$
$$= \int_A \{\sigma_{ii}^{\text{aux}}[\lambda_{ii,1}(\Delta T) + \lambda_{ii}T_{,1}]\}q\mathrm{d}A, \tag{56}$$

where λ_{ij} is related to the thermal expansion coefficient α_{ij}

$$\lambda_{11} = \alpha_{11};$$
$$\lambda_{22} = \alpha_{22}; \tag{57}$$
$$\lambda_{33} = \alpha_{33}; \lambda_{12} = 0,$$

For the plane stress state, the equation remains applicable. However, specific modifications to the equation are necessary for plane strain problems.

$$\lambda_{11} = \mu_{31}\alpha_{33} + \alpha_{11};$$
$$\lambda_{22} = \mu_{32}\alpha_{33} + \alpha_{23}; \tag{58}$$
$$\lambda_{33} = \alpha_{33}; \quad \lambda_{42} = 0,$$

where μ_{ij} denotes Poison's ratio.

The interaction integral M is linked to the SIF through the following equation:

$$M = 2c_{11}K_{\text{I}}^{\text{aux}}K_{\text{I}} + c_{12}(K_{\text{I}}^{\text{aux}}K_{\text{II}} + K_{\text{II}}^{\text{aux}}K_{\text{I}}) + 2c_{22}K_{\text{II}}^{\text{aux}}K_{\text{II}}, \tag{59}$$

$$c_{11} = -\frac{a_{22}}{2}\text{Im}\left(\frac{\mu_1 + \mu_2}{\mu_1\mu_2}\right), \tag{60}$$

$$c_{12} = -\frac{a_{22}}{2}\text{Im}\left(\frac{1}{\mu_1\mu_2}\right) + \frac{a_{11}}{2}\text{Im}(\mu_1\mu_2), \tag{61}$$

$$c_{22} = \frac{a_{11}}{2}\text{Im}(\mu_1 + \mu_2). \tag{62}$$

The SIF K_I and K_{II} can be determined by solving two simultaneous equations.

$$\begin{cases} M_1^l = 2c_{11}K_I + c_{12}K_{II} \\ (K_I^{aux} = 1 \text{ and } K_{II}^{aux} = 0) \\ M_2^l = c_{12}K_I + 2c_{22}K_{II} \\ (K_I^{aux} = 0 \text{ and } K_{II}^{aux} = 1). \end{cases} \qquad (63)$$

2.3 Stochastic response of MMSIF for different input random variables

This article explores the stochastic behavior of MMSIFs using the XIGA approach. It employs two probabilistic methods, namely SOPT, which relies on perturbation techniques, and direct MCS, a sampling-based method. SOPT, employing Taylor series expansion, establishes connections between certain features of random parameters and their corresponding responses. But, this method's applicability is confined because of its dependency on lower-order polynomials. The subsequent section provides a numerical formulation outlining these methods.

2.3.1 Monte Carlo simulation (MCS)

The direct MCS method simulates numerical experiments by generating numerous samples of random system properties, representing variability by using appropriate Gaussian distribution in structural parameters. These samples produce a random set of responses. The average of these random samples determines the mean response value, while their standard deviation (SD) indicates the variation, contingent on convergence. Despite being computationally intensive for solving structural issues involving discontinuities such as cracks, adopting adaptive sampling techniques can effectively address this challenge. The integral representing the expected value transforms into an averaging operator is

$$\overline{\mu}_f = E[f(x)] = \frac{1}{N} \sum_{i=1}^{N} f(x_i), \qquad (64)$$

where $\overline{\mu}_f$ is the mean or expected value (E) of a function $f(x)$ of n-dimensional random variable vector x. The parameter N is known as a set of random samples. The N samples must be drawn from a distribution specified by $\varphi(x)$, which can be either normal or lognormal.

Random function $f(x)$ variance can be

$$\sigma_f^2 = \text{Var}[f(x)] = \int_{\Omega} (f(x) - \mu_f)^2 \phi(x) dx. \qquad (65)$$

When the above integral is calculated in Monte Carlo simulations using sampled data, the following summation can be used in its place

$$\sigma_f^2 = \text{Var}[f(x)] = \frac{1}{N-1} \sum_{i=1}^{N} (f(x_i) - \mu_f)^2. \qquad (66)$$

Difficulty with this method is creating random sample points which mimic the distribution pattern of the integrand. In this study, we've taken 3,000 samples ($N = 3{,}000$) to ensure convergence, addressing the complexity of the fracture problem at hand.

2.3.2 Second-order perturbation technique (SOPT)

A response variable $f(K_i)$ of MMSIFs (K_I or K_{II}) is defined by

$$K = f(K_i) \text{ where } i = I, II, \qquad (67)$$

where K_i represents functions of random variables b_j, which can be statistically dependent or independent, correlated or uncorrelated. These variables possess mean μ_{b_j} and standard deviation σ_{b_j}

$$\text{if } i = I \text{ then } K_I = K_I \qquad (68)$$

$$\text{if } i = II \text{ then } K_{II} = K_{II}. \qquad (69)$$

Using Taylor series expansion till second-order K_i is expanded around mean values of random variables μ_{b_1}, $\mu_{b_2},..., \mu_{b_n}$, allowing the determination of mean values of MMSIFs K_I K_{II}

$$K = K_i(\mu_{b_1}, \mu_{b_2}, ..., \mu_{b_n}) + \sum_{j=1}^{n} (x_j - \mu_{b_j}) \frac{\partial K_i}{\partial b_j}$$
$$+ \frac{1}{2} \sum_{j=1}^{n} \sum_{k=1}^{n} (x_j - \mu_{b_j})(x_k - \mu_{b_k}) \frac{\partial^2 K_i}{\partial b_j b_k}. \qquad (70)$$

The first-order mean of K_I or K_{II} is defined as:

$$E(K_i') \approx K_i(\mu_{b_1}, \mu_{b_2}, ..., \mu_{b_n}). \qquad (71)$$

The first-order variance of mean K of SIFs K_I or K_{II}, written as Var(K'), is given as [51]

$$\text{Var}(K') = \sum_{j=1}^{n} \sum_{k=1}^{n} \frac{\partial K}{\partial b_i} \frac{\partial K}{\partial b_j} \text{Cov}(b_j, b_k). \qquad (72)$$

where Cov (b_j, b_k) is the covariance of b_j and b_k, and n is the total number of random variables.

Matrix of random variable covariance can be given as [38]

$$\text{cov}(b_j, b_k) = [C][C'], \qquad (73)$$

$$[C] = \begin{bmatrix} \sigma_{b_1}^2 & \mathrm{cov}(b_1, b_2) & ... & \mathrm{cov}(b_1, b_j) \\ \mathrm{cov}(b_2, b_1) & \sigma_{b_2}^2 & ... & \mathrm{cov}(b_2, b_j) \\ ... & ... & ... & ... \\ \mathrm{cov}(b_j, b_1) & \mathrm{cov}(b_j, b_2) & ... & \sigma_{b_j}^2 \end{bmatrix}, \quad (74)$$

$$[C'] = \begin{bmatrix} 1 & \rho_{b_1,b_2} & ... & \rho_{b_1,b_j} \\ \rho_{b_2,b_1} & 1 & ... & \rho_{b_2,b_j} \\ ... & ... & ... & ... \\ \rho_{b_j,b_1} & \rho_{b_j,b_2} & ... & 1 \end{bmatrix}. \quad (75)$$

Matrix of standard deviation is denoted by $[C]$, and correlation coefficient of the random variables is denoted by $[C']$ where:

$$\sigma_{X_1}, \sigma_{X_2}, ..., \sigma_{X_j} = \mathrm{cov}(b_j, b_k)\, X(\mu_{b_1}, \mu_{b_2}, ..., \mu_{b_j}), \quad (76)$$

$$\rho_{X_j,X_k} = \frac{\mathrm{cov}(b_j, b_k)}{\sigma_{b_j}\sigma_{b_k}}. \quad (77)$$

The covariance between the random variables is represented by the covariance $\mathrm{cov}(b_j, b_k)$. This covariance is 0 for random variables that are statistically independent. The degree of correlation between the random variables is indicated by the correlation coefficient $\rho bj, bk$, which can be taken to have any value.

Second-order mean $\{K''\}$ in SOPT given by [51]

$$E(K_i'') = K_i(\mu_{b_1}, \mu_{b_2}, ..., \mu_{b_n}) + \frac{1}{2}\mathrm{var}\{K_i'\}. \quad (78)$$

Second-order variance matrix of response $\mathrm{var}\{K_1''\}$

$$\mathrm{var}\{K_i''\} = \mathrm{var}\{K_i\}. \quad (79)$$

In various engineering scenarios, relying on the mean of second-order and variance of first order is customary since the unavailability of third- and fourth-order moments for estimating second-order variance of b_j [51] The coefficient of variance (COV) for Stress Intensity Factors (SIFs) is computed by dividing the standard deviation by the mean, with standard deviation derived from variance's square root.

The perturbation technique used in this analysis offers computational efficiency, making it adaptable to a wide range of probabilistic problems. However, its limitation lies in its suitability for scenarios with lower variability in random variables, particularly where randomness is minimal compared to their mean values. To address this limitation, Monte Carlo Simulation (MCS) emerges as an optimal method for computing response statistics, especially in cases with significant uncertainties. Although computationally intensive, particularly in fracture problems with dense meshes, MCS remains preferable for handling larger uncertainties [52].

3 Results and discussion

This section introduces many of the classical numerical examples implemented through a MATLAB-based code for the extended isogeometric analysis algorithm along with the stochastic responses. The significance of MMSIFs in fracture analysis under mechanical and thermomechanical loadings is emphasized by prior research studies. First, the validation of the MATLAB code for the XIGA algorithm is checked by calculating MMSIFs and comparing them with the available works of literature. Afterward, the study conducts numerical experiments in various scenarios to calculate the mean and coefficient of variance of MMSIFs in orthotropic plates with centrally inclined cracks subjected to thermomechanical loads. This analysis involves considering random input variables like elastic properties, crack angle, and crack length, temperature both independently and in combination, as random variables.

3.1 Edge crack with various orientations of orthotropic axis subjected to tensile loading

We apply the proposed method to analyze an edge crack in a rectangular plate. The plate has a height-to-width ratio of 2 and a crack length-to-width ratio of 0.45, as shown in Figure 3(a). The material used is graphic epoxy with properties that are described below:

E_1 = 114.8 GPa, E_2 = 11.7 GPa, G_{12} = 9.66 GPa and μ_{12} = 0.21.

The mesh features a uniform distribution of nodes in extended isogeometric analysis. NURBS basis functions employed are ($p = q = 3$) cubic, as depicted in Figure 3(b), with enriched nodes shown in Figure 3(c). The integral domain for calculating SIF is illustrated. Our results are compared with Aliabadi and Mohammadi. Figure 4 presents the SIF values for various α angles, obtained using the proposed XIGA method, Aliabadi's FEM, and Mohammadi's XFEM analyses.

The maximum difference in mode I SIF is observed at $\alpha = 0°$ where a 4.3% error is observed, and for mode II, this occurs when $\alpha = 20°$ where a 3.6% error is observed. The results obtained by this method demonstrate that for both modes, there is an increase in normalized SIF value from $\alpha = 0°$ to $\alpha = 45°$ and then are decreased from $\alpha = 45°$ to $\alpha = 90°$.

The effect of crack length on K_I and K_{II} was investigated for $\alpha = 0°$ orientation which is shown in Table 1
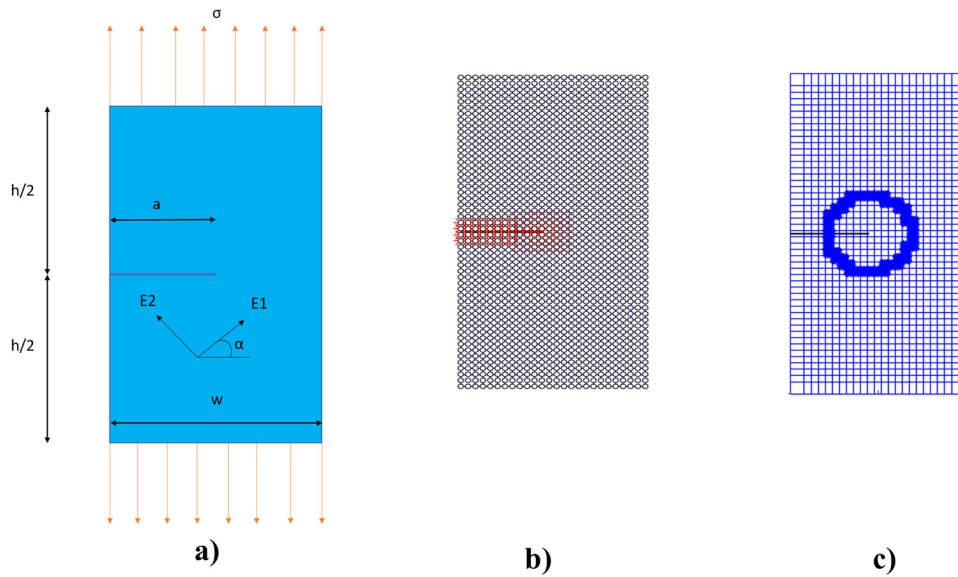
Figure 3: (a) The loading and geometry for a single edge crack with various orientations of orthotropic axis in rectangular plate, (b) NURBS mesh with enriched nodes, and (c) integral domain to calculate SIF.
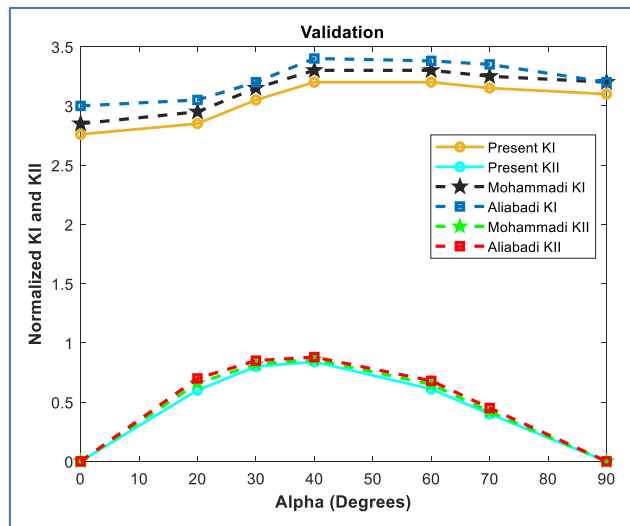

Figure 4: Results of normalized SIFs for K_I and K_{II} of a single edge crack in a rectangular plate with various orientations of the orthotropic axes, at angles of α = 0° 30° 45° 60° 90° and ($\overline{K_I} = K_I/\sigma\sqrt{\pi a}$ and $\overline{K_{II}} = K_{II}/\sigma\sqrt{\pi a}$).

Table 1: Effect of crack length on values of SIF, K_I, and K_{II}

Crack length	K_I	K_{II}
2.5	1.4672	-2.0000×10^{-5}
3.5	1.9525	-4.0000×10^{-5}
4.5	2.6012	-7.0000×10^{-5}
5.5	3.4990	-6.0000×10^{-5}
6.5	4.7486	-4.0000×10^{-5}
7.5	6.0173	-1.0000×10^{-5}

below which shows an exponential increment in K_I with an increase in crack length, and minor variation was found in K_{II} values.

Further study was carried out for different loading on the top edge of the plate (Tensile, Shear, Combined, and Triangular), and values of Normalized SIF, K_I, and K_{II} were recorded for different orientation angles (α = 0° to α = 90°), which are presented in Table 2.

The crack length taken into consideration was a/w = 0.45 and h/w = 2 as depicted in Figure 3(a), and values of K_I opening mode are more in combined loading as compared with only shear loading which is more than only tensile loading for all orientation angles. K_{II} shearing mode was very low in tensile loading but in shear and combined loading it was comparatively higher for all the orientation angles. For a triangular tensile load, it was obvious that the values of K_I and K_{II} would give lower values as the total load was half that of the uniformly distributed load.

Results of normalized K_I and K_{II} for different orientation angles under tensile, shear, and combined loading are depicted in Figures 5–7.

3.2 Isotropic plate with center crack under thermomechanical loading
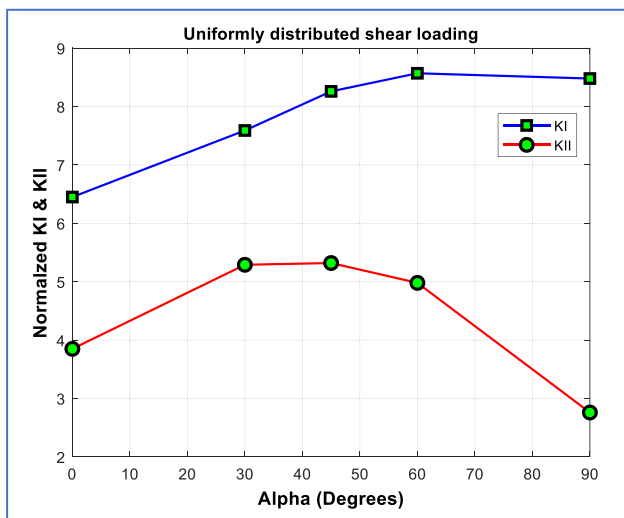
Here, we investigate a square plate with a center crack through numerical simulations under thermomechanical loading, employing the XIGA approach. The dimensions considered are 2,000 mm × 2,000 mm, and the domain is

Table 2: Values of normalized SIF under different loading conditions – tensile, shear, combined, and triangular are recorded for different orientation angle

Alpha (orthotropic angle)	TENSILE		SHEAR		COMBINED		TRIANGULAR	
	K_I	K_{II}	K_I	K_{II}	K_I	K_{II}	K_I	K_{II}
0	2.6012	0	6.4557	3.8599	9.0569	3.8598	1.7945	0
30	2.8256	0.3935	7.5976	5.2948	10.4231	5.6883	1.9894	0.3352
45	2.9946	0.4689	8.2649	5.3205	11.2595	5.7893	2.1355	0.4011
60	3.0765	0.3695	8.5767	4.9892	11.6533	5.3587	2.2111	0.3295
90	3.0267	−0.134	8.4802	2.7663	11.5069	2.6315	2.1735	−0.111
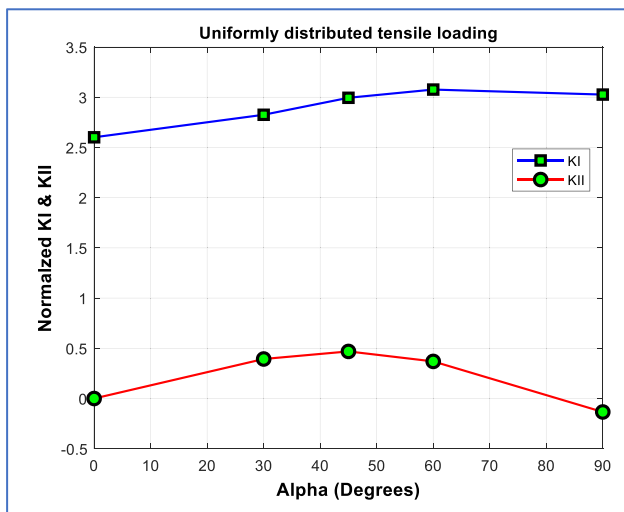
Figure 5: Normalized K_I & K_{II} for different orientation angles under tensile loading.

discretized using a 50 × 50 control net. We use a NURBS basis function order of three for the simulations.

The plate contains a preexisting center crack with a length of 600 mm, as shown in Figure 8. The material properties considered are as follows:

- elastic modulus (E) = 200 GPa;
- Poisson ratio (v) = 0.3;
- thermal expansion coefficient (α) = 11.7 × 10^{-6} C^{-1}.

The scenario involves a square plate under tensile load of 30 MPa applied at the top edge which is perpendicular to the crack. Additionally, temperature boundary conditions are applied: 0°C at the crack face and 10°C at the top edge of the plate. The bottom edge of the plate is constrained, as depicted in Figure 8.

For each step of crack extension, a crack increment of 100 mm is applied, extending proportionally from both the left and right tips. The stress intensity factors are then calculated using the domain-based interaction integral approach.

Figure 9 illustrates the stresses in x-direction (u_x) for a/w = 0.4 subjected to thermomechanical loads, while Figure 10 shows stresses in the y-direction. Additionally,

Figure 6: Normalized K_I & K_{II} for different orientation angles under shear loading.
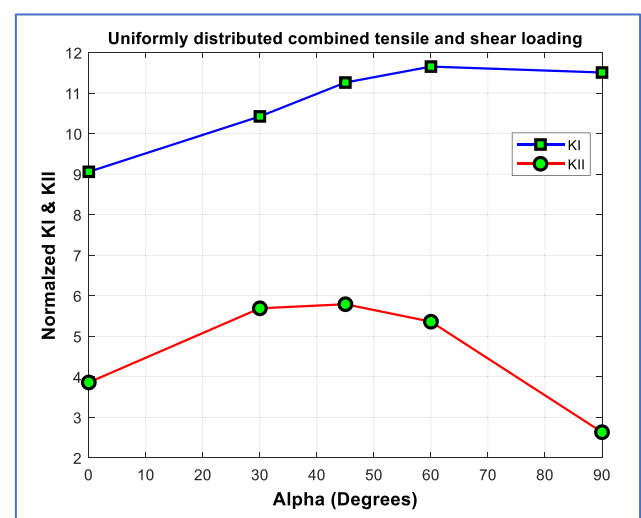
Figure 7: Normalized K_I & K_{II} for different orientation angles for combined tensile and shear loading.
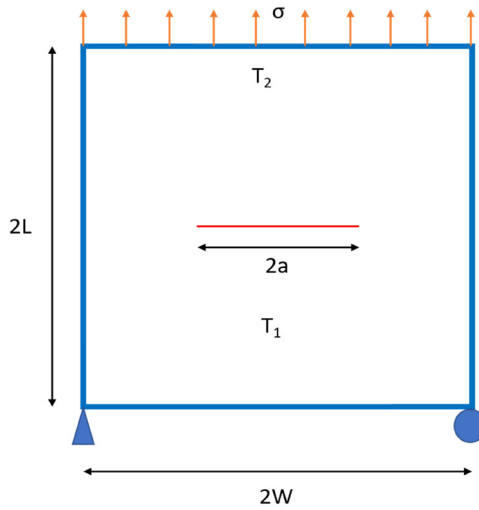
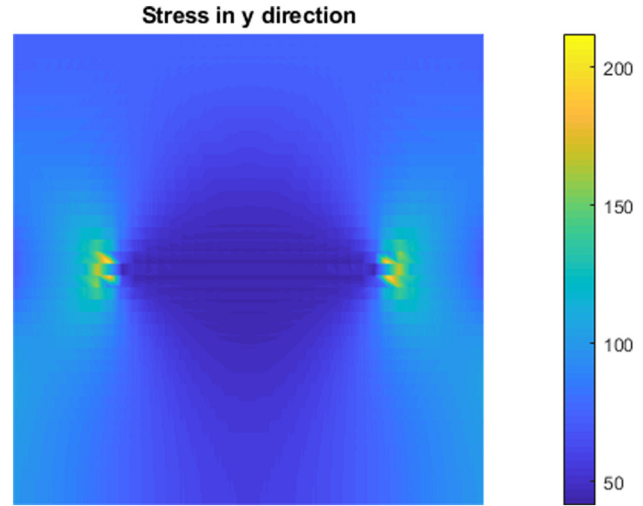**Figure 8:** Center cracked square plate under thermomechanical loading.

Figure 10: Stresses along y-axis.

Figures 11 and 12 display the displacements along the x direction and y direction. The variation of SIFs (K_I and K_II) with the extension of the right crack tip is shown in Figure 13. The graph indicates that K_I is higher than K_II. Consequently, under combined loading conditions, the center crack in the plate exhibits opening mode behavior.

3.3 Orthotropic plate with center crack under mechanical, thermal, and thermomechanical uniaxial loading

We further analyze a center crack in a square plate under thermomechanical loads, using the XIGA approach for an orthotropic material. The square plate has initial dimensions of 2,000 mm × 2,000 mm, and the domain is discretized using a control net of size 50 × 50.
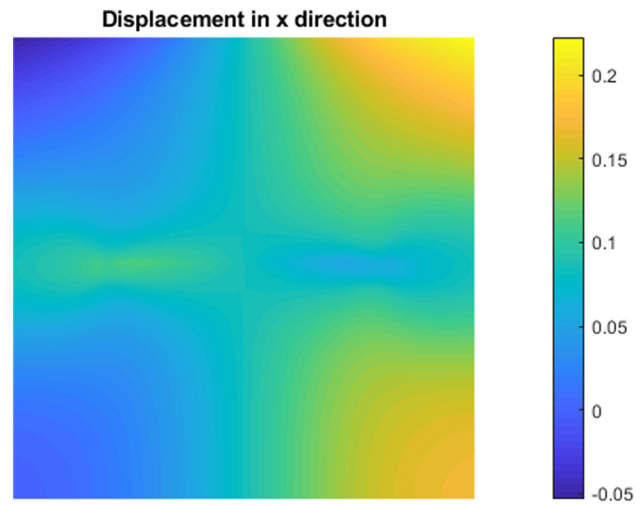
Figure 11: Displacement along x-axis.
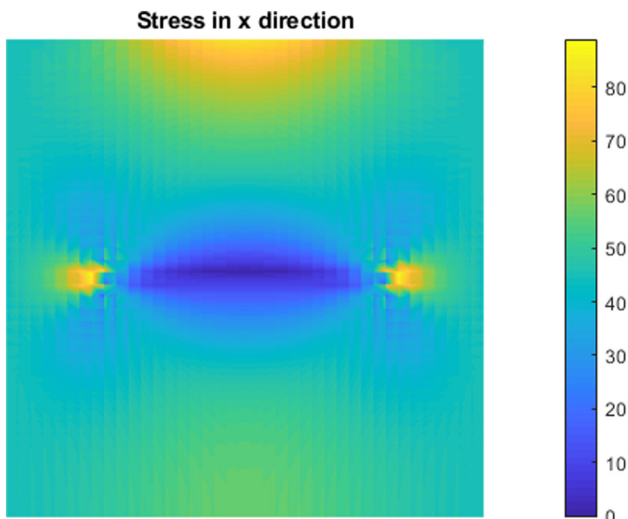
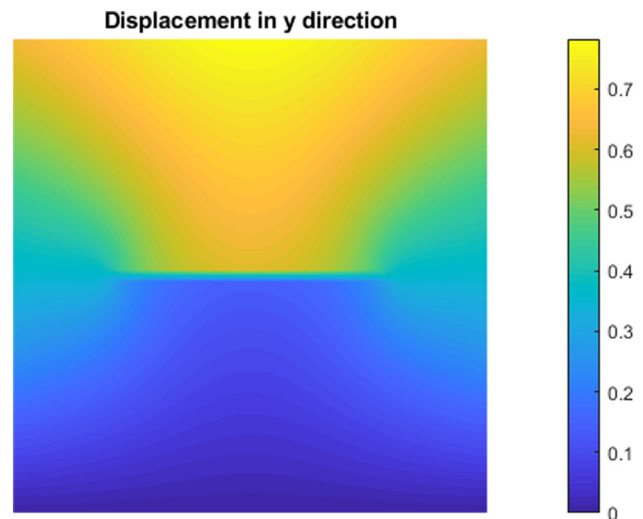**Figure 9:** Stresses along x-axis.

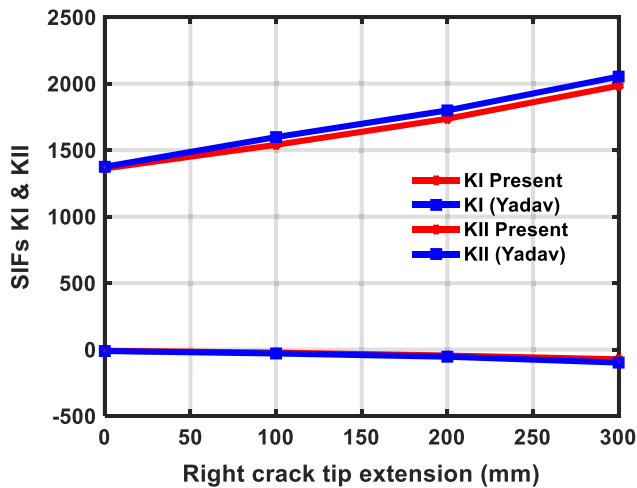**Figure 12:** Displacement along y-axis.

Figure 13: SIFs (K_I and K_{II}) variation of the plate subjected to thermomechanical loads is presented (validation study).

Figure 14: Center-cracked orthotropic square plate under thermomechanical loading.

The square plate contains a preexisting center crack with a length of 600 mm, as depicted in Figure 14. This crack is analyzed when subjected to thermomechanical loading conditions using the XIGA method. The material properties considered for the analysis are as follows:
- elastic modulus ($E11$) = 114.8 GPa;
- elastic modulus ($E22$) = 11.7 GPa;
- shear modulus ($G12$) = 9.66 GPa;
- Poisson ratio ($\nu12$) = 0.21;
- thermal expansion coefficient ($\alpha11$) = 11.7 × 10^{-6} C^{-1};
- thermal expansion coefficient ($\alpha22$) = 2 × 10^{-5} C^{-1}.

Boundary conditions are as follows:
- temperature difference = 100°C;
- tensile stress on top edge = 30 MPa.

Table 3 presents the normalized SIF, K_I and K_{II}, for different crack lengths. The results show that K_I is consistently higher than K_{II}. This indicates that the center crack in the square plate primarily experiences opening mode under combined loading conditions, even for orthotropic materials. Furthermore, the analysis suggests that thermomechanical loading is more critical than pure mechanical or pure thermal loading. This is supported by the observation that as the crack length increases, the SIF values increase for all loading types.

3.4 Orthotropic center crack under mechanical, thermal, and thermomechanical biaxial loading

Here, we analyze a center crack in a square plate under thermomechanical biaxial loading, utilizing the XIGA approach.
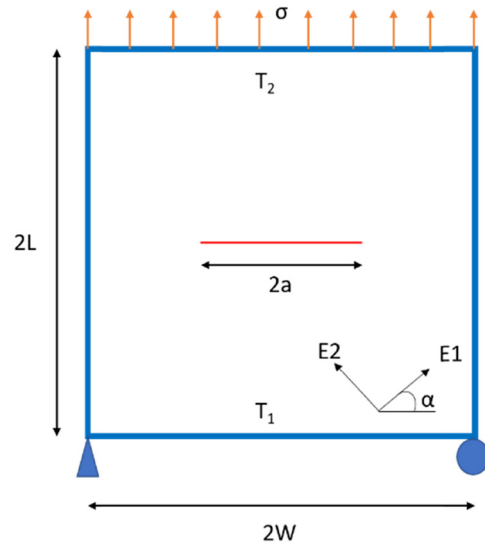
The material properties remain the same as in the previous section, and the geometry and loading conditions are illustrated in Figure 15. The boundary conditions for this analysis are as follows:
- Temperature difference = 100°C;
- Tensile stress on top edge = 30 MPa;
- Tensile stress on right edge = 60 MPa.

The normalized SIFs (K_I and K_{II}) with the different crack lengths is shown in Table 4. It is observed that the value of K_I (mode-I) is higher than that of K_{II} (mode-II). Also, the K_I (mode-I) SIF value is reduced when subjected to biaxial tensile loading, and K_{II} (mode-II) SIF value is increased when both are compared with uniaxial tensile loading. Apart from this behavior, the critical loading condition remains the same with thermomechanical loading which gives higher values of SIF K_I than pure thermal and pure mechanical.

Table 3: SIF K_I and K_{II} for mechanical, thermal, and thermomechanical loading for different crack length

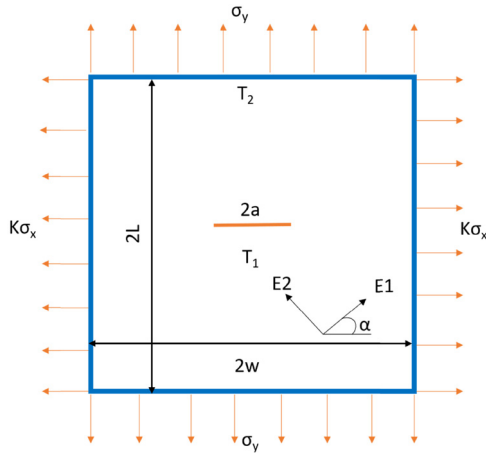| Half crack length	Mechanical (uniaxial tension)		Thermal		Thermomechanical (uniaxial tension)	
	K_I	K_{II}	K_I	K_{II}	K_I	K_{II}
300	19.8675	−0.0460	1.2013	0.0	21.0688	−0.0460
400	21.5581	−0.0687	4.7554	0.0	26.3135	−0.0687
500	24.4024	−0.0881	4.5680	0.0	28.9705	−0.0881
600	27.7666	−0.1101	4.3658	0.0	32.1324	−0.1101

Figure 15: Cracked orthotropic square plate under thermomechanical biaxial tensile loads.

Table 4: Stress intensity factors K_I and K_{II} for mechanical, thermal, and thermomechanical biaxial tensile loadings for different crack length

Half crack length	Mechanical (biaxial tension)		Thermal		Thermomechanical (biaxial tension)	
	K_I	K_{II}	K_I	K_{II}	K_I	K_{II}
300	14.0576	−0.0460	1.2013	0.0	15.2589	−0.0460
400	14.8412	−0.0687	4.7554	0.0	19.5966	−0.0687
500	17.8220	−0.0881	4.5680	0.0	22.3900	−0.0881
600	21.3245	−0.1101	4.3658	0.0	25.6903	−0.1101

Further study is carried out with shear loading instead of tensile loading on the same geometry, and the same material property is shown in Figure 16 with loading conditions as:

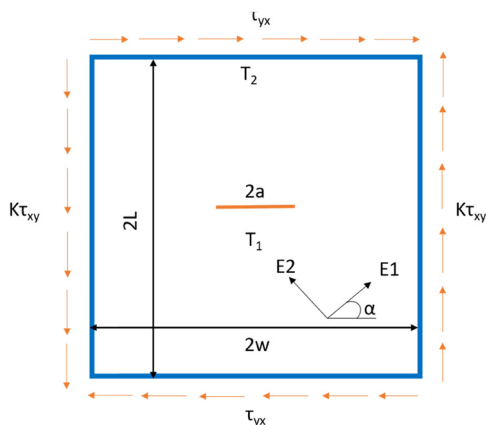Shear stress on top and right edges = 30 MPa and 60 MPa.

Figure 16: Cracked orthotropic square plate under thermomechanical biaxial shear loads.

Table 5: Stress intensity factors K_I and K_{II} for mechanical, thermal, and thermomechanical biaxial shear loading for different crack lengths

Half crack length	Mechanical (biaxial shear)		Thermal		Thermomechanical (biaxial shear)	
	K_I	K_{II}	K_I	K_{II}	K_I	K_{II}
300	15.5137	18.3029	1.2013	0.0	16.7150	18.3029
400	16.1450	20.4201	4.7554	0.0	20.9004	20.4201
500	18.0810	22.1619	4.5680	0.0	22.6490	22.1619
600	20.4881	23.4087	4.3658	0.0	24.8539	23.4087

The normalized SIFs (K_I and K_{II}) with the different crack lengths are shown in Table 5. It is observed that the value of K_{II} (mode-II) is higher than K_I (mode-I). Therefore, the center crack in the square plate induces shearing mode (mode-II) under mechanical and thermomechanical loading conditions for orthotropic properties. It is observed that K_I (mode-I) SIF and K_I (mode-I) SIF values are increased when subjected to biaxial shear when compared with biaxial tensile loading. Apart from this behavior, the critical loading condition remains the same with thermomechanical loading which gives higher values of SIF K_I than pure thermal and pure mechanical (shear).

Now, the investigation is carried out with thermomechanical biaxial tensile, thermomechanical biaxial shear, and thermomechanical biaxial combined tensile and shear loading for half crack angles of 300, 400, 500, and 600 mm depicted in Figure 17 along with the variation of load factor $K = 1, 2,$ and 4, and the results of mixed mode SIF are shown in Table 6.

Figures 18 and 19 show K_I and K_{II}, respectively, for different load factors K. It is seen that for all the cases, combined loading is dominant irrespective of load factor K. For K_I values: tensile load is dominant at load factor $K = 1$, shear load is dominant at load factor $K = 4$, and it is almost same at load factor $K = 2$. For K_{II} values, the tensile load has zero irrespective of the load factor; therefore, shear and combined cases show the same value of K_{II} for all load factors.

3.5 Stochastic response of orthotropic center crack under mechanical, thermal, and thermomechanical biaxial loading

Exploring the unpredictable behavior of orthotropic plates containing cracks under mechanical, thermal, and thermomechanical biaxial loading using XIGA provides valuable insights into complex structural behavior. These investigations aid in the creation of more secure and dependable engineering designs across diverse applications. Understanding the
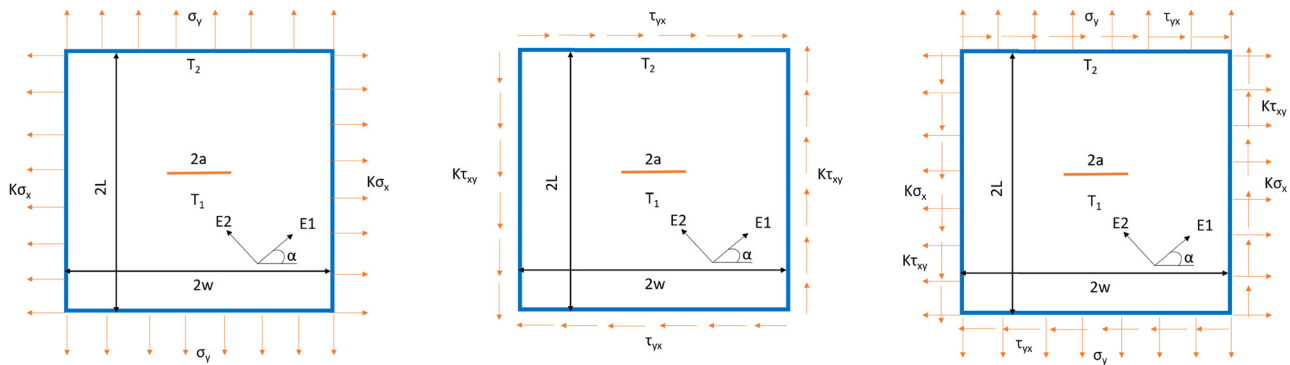
Figure 17: Center cracked orthotropic square plate subjected to thermomechanical biaxial tensile, biaxial shear and biaxial combined loading.

probabilistic responses of such structures helps enhance their reliability and safety measures. The stochastic response was observed using identical material properties previously discussed, employing a half crack length of 300 and different load factors K = 1, 2, and 4.

Table 7 presents a comparative analysis of the normalized mean and COV of the MMSIF. These were derived through both the SOPT and MCS. The primary objective was to validate the accuracy of the stochastic XIGA algorithm by comparing SOPT outcomes against MCS results.

The findings reveal a high level of agreement between the current SOPT outcomes and those from MCS, implemented directly in MATLAB. Notably, the input random

Table 6: K_I and K_{II} for half crack length 300, 400, 500, and 600 with variation of load factor K = (1, 2 and 4) under thermomechanical biaxial tension, thermomechanical biaxial shear, and thermomechanical biaxial tension and shear

Half crack length = 300	Thermomechanical (biaxial tension)		Thermomechanical (biaxial shear)		Thermomechanical (biaxial tensile and shear)	
Load factor	K_I	K_{II}	K_I	K_{II}	K_I	K_{II}
1	18.1638	−0.0460	10.1230	6.9288	27.0856	6.8828
2	15.2589	−0.0460	16.7150	18.3029	30.7726	18.2569
4	9.4490	−0.0460	29.8989	41.0511	38.1466	41.0051

Half crack length = 400	Thermomechanical (biaxial tension)		Thermomechanical (biaxial shear)		Thermomechanical (biaxial tensile and shear)	
Load factor	K_I	K_{II}	K_I	K_{II}	K_I	K_{II}
1	22.9550	−0.0687	14.2439	7.7033	32.4435	7.6346
2	19.5966	−0.0687	20.9004	20.4201	35.7416	20.3514
4	12.8797	−0.0687	34.2135	45.8537	42.3377	45.7849

Half crack length = 500	Thermomechanical (biaxial tension)		Thermomechanical (biaxial shear)		Thermomechanical (biaxial tensile and shear)	
Load factor	K_I	K_{II}	K_I	K_{II}	K_I	K_{II}
1	25.6802	−0.0881	15.3253	8.3456	36.4375	8.2575
2	22.3900	−0.0881	22.6490	22.1619	40.4710	22.0738
4	15.8096	−0.0880	37.2963	49.7945	48.5378	49.7065

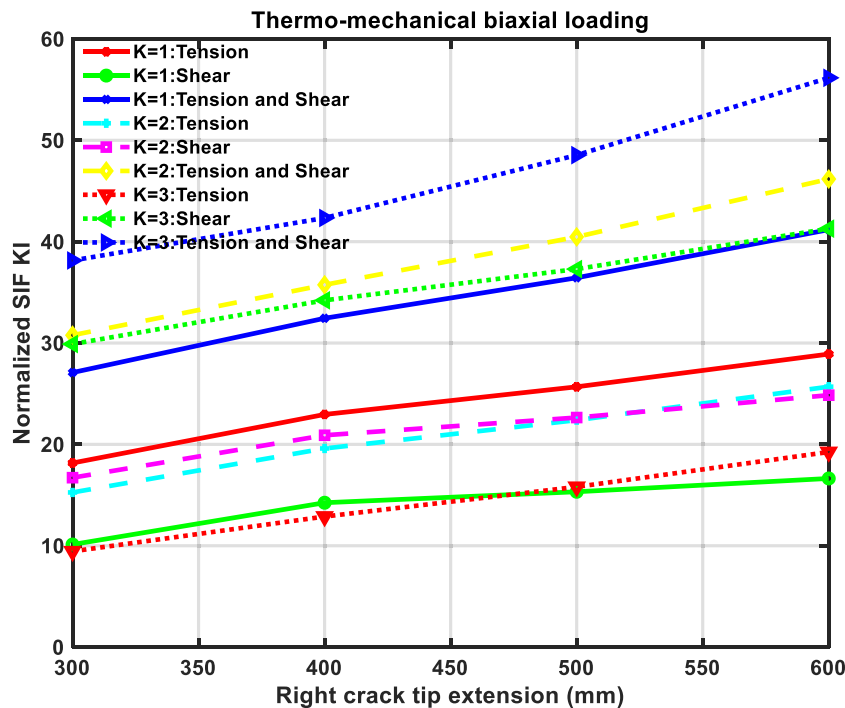| Half crack length = 600	Thermomechanical (biaxial tension)		Thermomechanical (biaxial shear)		Thermomechanical (biaxial tensile and shear)	
Load factor	K_I	K_{II}	K_I	K_{II}	K_I	K_{II}
1	28.9114	−0.1101	16.6390	8.8243	41.1845	8.7142
2	25.6903	−0.1101	24.8539	23.4087	46.1784	23.2986
4	19.2482	−0.1101	41.2838	52.5775	56.1662	52.4674

Figure 18: Comparison of K_I values for thermo mechanical loading with variation of load factor and type of mechanical loading.

parameter considered for variation was solely the crack length, at 0.2 or 20%.

In Table 7, crack length is taken as the random input parameter with COV = 0.2, mean values of K_I decrease with an increase in load factor for thermomechanical (Biaxial Tension) but COV values increase with an increase in load factor. K_{II} can be neglected for biaxial tension as it is very close to zero.

In thermomechanical biaxial shear loading mean values are increasing for K_I and COV values are decreasing with an
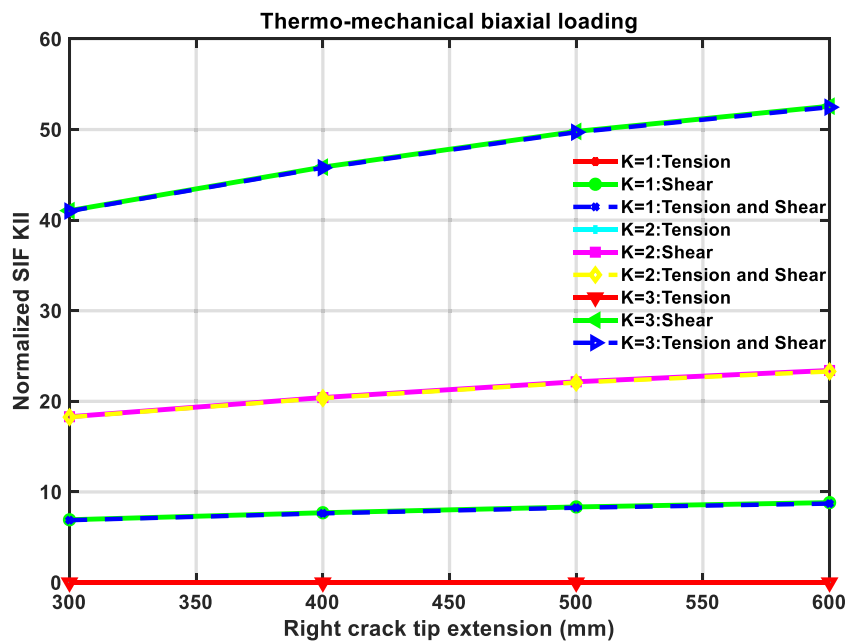

Figure 19: Comparison of K_{II} values for thermomechanical loading with variation of load factor and type of mechanical loading.

Table 7: Variation of mean and COV for different values of load factor K when crack length is the only random input parameter under biaxial thermomechanical (tensile, shear, and combined) loading

Half crack length = 300	Stochastic method	SIF	Thermomechanical (biaxial tension)		Thermomechanical (biaxial shear)		Thermomechanical (biaxial tensile and shear)	
COV = 0.2 Load factor K			Mean	COV	Mean	COV	Mean	COV
1	SOPT	K_I	18.1638	0.0051	10.1230	0.0770	27.0856	0.0271
		K_{II}	−0.0460	−0.2261	6.9288	0.0431	6.8828	0.0419
2		K_I	15.2589	0.0119	16.7150	0.0275	30.7726	0.0372
		K_{II}	−0.0460	−0.2262	18.3029	0.0482	18.2569	0.0478
4		K_I	9.449	0.0381	29.899	0.0060	38.1466	0.0514
		K_{II}	−0.0460	−0.2262	41.051	0.0500	41.005	0.0498
1	MCS	K_I	18.5326	0.0055	10.2135	0.0753	28.7499	0.0235
		K_{II}	−0.0510	−0.2273	6.9865	0.0459	6.9355	0.0433
2		K_I	15.7593	0.0128	16.8365	0.0256	32.5932	0.0351
		K_{II}	−0.0510	−0.2277	18.4005	0.0497	18.3495	0.0459
4		K_I	9.6983	0.0389	29.9265	0.0059	39.6296	0.0525
		K_{II}	−0.0510	−0.2259	41.1253	0.0568	41.0743	0.0513

increase in load factor. Both mean and COV values increase for K_{II}. In the case of thermomechanical (Biaxial Tensile and Shear) loading both mean and COV values are increasing with an increase in load factor for K_I as well as K_{II}.

In Table 8, the temperature difference is taken as the input random variable at COV = 0.2 for different loadings, and it is seen that maximum COV in K_{II} values of thermomechanical (Biaxial Tensile and Shear) loading case. Also, these values are mostly close to 0.2 which is our input random value for temperature difference. The COV for K_I is also close to 0.2 which infers that temperature variation does not impact both K_I and K_{II} values that much.

From Table 9, it is observed that COV values are decreasing and mean values are increasing with increasing crack length values for K_I. For biaxial tensile loading, K_{II} values are negligible. COV values ranging from 0.3384 to 0.3973 are observed in shear and combined loading.

From Table 10, it is seen that COV values for K_I are constantly between 0.3032 and 0.3973 for combined loading and tensile loading but for shear loading, it is much more than that (0.3894 and 0.6128).

For K_{II}, COV values are constant at 0.3940 for shear and 0.3973 for combined loading with an increase in temperature which shows there is no effect of temperature on K_{II} values. Mean values decrease with an increase in temperature difference for K_I and K_{II} in the case of tensile, shear, and combined loading.

4 Concluding remarks

The concept of IGA aims to unify the representation of computational domain for both geometry & field variables,

Table 8: Variation of mean and COV for different values of load factor K when temperature is the only random input parameter under biaxial thermomechanical (tensile, shear, and combined) loading

Half crack length = 300	SIF	Thermomechanical (biaxial tension)		Thermomechanical (biaxial shear)		Thermomechanical (biaxial tensile and shear)	
COV = 0.2 Load factor K		Mean	COV	Mean	COV	Mean	COV
1	K_I	18.1638	0.1946	10.1230	0.1836	27.0856	0.1991
	K_{II}	−0.0460	−0.2083	6.9288	0.2083	6.8828	0.2083
2	K_I	15.2589	0.1919	16.7150	0.1934	30.7726	0.2002
	K_{II}	−0.0460	−0.2083	18.3029	0.2083	18.2569	0.2083
4	K_I	9.4490	0.1818	29.899	0.2000	38.1466	0.2018
	K_{II}	−0.0460	−0.2083	41.051	0.2083	41.005	0.2083

Table 9: Effect of crack length on the normalized mean and COV of K_I and K_{II} under biaxial tensile, shear, and combined thermomechanical loading (crack length, crack angle, Delta T, E1, E2, and nu1 are taken as input random parameters)

Crack angle = 90 Load factor = 1 COV = 0.2 Delta T = 100		Thermomechanical (biaxial tension)		Thermomechanical (biaxial shear)		Thermomechanical (biaxial tensile and shear)	
		Mean	COV	Mean	COV	Mean	COV
Crack length = 300	K_I	18.1638	0.4312	10.1230	0.6128	27.0856	0.3896
	K_{II}	−0.0460	−0.0849	6.9288	0.3940	6.8828	0.3973
Crack length = 400	K_I	22.9550	0.1938	14.2439	0.1648	32.4435	0.2357
	K_{II}	−0.0687	−0.0239	7.7033	3587	7.6346	0.3617
Crack length = 500	K_I	25.6802	0.1280	15.3253	0.1616	36.4375	0.1451
	K_{II}	−0.0881	−0.0814	8.3456	0.3339	8.2575	0.3384
Crack length = 600	K_I	28.9114	0.0962	16.6390	0.2620	41.1845	0.0696
	K_{II}	−0.1101	−0.1019	8.8243	0.3773	8.7142	0.3833

streamlining the integration of CAD and CAE industries. Over the past few years, Extended Isogeometric Analysis (XIGA) has demonstrated significant potential as a prospective alternative in the field of computational fracture analysis.

The stochastic XIGA using SOPT and FOPT is applied for the calculation of mean and COV of normalized MMSIF of the orthotropic plate with a central crack under thermomechanical loading and the results are in good agreement with MCS results.

The variability in crack length and crack angle, as random factors, significantly surpasses other variables in impacting the safety and reliability of orthotropic plates under thermomechanical loads. Thus, maintaining precise control over these factors becomes crucial to ensure reliability and structural integrity.

For an orthotropic plate with a center crack under mechanical, thermal, and thermomechanical uniaxial loadings, it is found that the SIF values increase with the increase in half crack length, and the maximum K_I

value is 32.13 at 600 half crack length when subjected to thermomechanical uniaxial tensile load. The SIF value under pure thermal loading is minimal as compared to mechanical loading values.

In an orthotropic center crack under thermomechanical biaxial loading, K_I values decrease with an increasing load factor under biaxial tensile load, while both K_I and K_{II} values increase under biaxial shear loading as the load factor rises. This indicates that thermomechanical biaxial shear loading requires careful monitoring at higher biaxial load factors to ensure the safety and reliability of the plates. Combined loading (thermomechanical biaxial tensile and shear) results in maximum values at all crack lengths, necessitating extra caution to ensure the plate's safety under such conditions.

The present work can also be expanded on the curved cracks which can be modeled and predicted more accurately using the XIGA methodology. Also, the inclusion of machine learning algorithms to predict crack initiation and propagation more accurately and efficiently is a

Table 10: Effect of temperature difference on the normalized mean and COV of K_I and K_{II} under biaxial tensile, shear, and combined thermomechanical loading (crack length, crack angle, Delta T, E1, E2, and nu1 are taken as input random parameters)

Crack length = 300 Crack angle = 90 Load factor = 1 COV = 0.2		Thermomechanical (biaxial tension)		Thermomechanical (biaxial shear)		Thermomechanical (biaxial tensile and shear)	
		Mean	COV	Mean	COV	Mean	COV
Delta T = 25	K_I	69.0516	0.3024	36.8883	0.3894	104.7386	0.3032
	K_{II}	−0.1842	−0.0849	27.7154	0.3940	27.5312	0.3973
Delta T = 50	K_I	35.1264	0.3468	19.0448	0.4685	52.9700	0.3327
	K_{II}	−0.0921	−0.0849	13.8577	0.3940	13.7656	0.3973
Delta T = 75	K_I	23.8180	0.3897	13.0969	0.5429	35.7137	0.3614
	K_{II}	−0.0614	−0.0849	9.2385	0.3940	9.1771	0.3973
Delta T = 100	K_I	18.1638	0.4312	10.1230	0.6128	27.0856	0.3896
	K_{II}	−0.0460	−0.0849	6.9288	0.3940	6.8828	0.3973

potential advancement. Enhanced material models incorporating non-linear behavior and multi-physics interactions would improve the simulation of real-world conditions.

Author contributions: Authors have accepted responsibility for the entire content of this manuscript and consented to its submission to the journal, reviewed all the results, and approved the final version of the manuscript. AL and NMK developed the model code. NMK performed the simulations and prepared the manuscript with contributions from co-author.

Conflict of interest: The authors state no conflict of interest.

Data availability statement: All data generated and analyzed during this study are included in this article.

References

[1] Viola E, Piva A, Radi E. Crack propagation in an orthotropic medium under general loading. Eng Fract Mech. 1989;34(5–6):1155–74. doi: 10.1016/0013-7944(89)90277-4.

[2] Nobile L, Carloni C. Fracture analysis for orthotropic cracked plates. Compos Struct. 2005;68(3):285–93. doi: 10.1016/j.compstruct.2004.03.020.

[3] Lim WK, Choi SY, Sankar BV. Biaxial load effects on crack extension in anisotropic solids. Eng Fract Mech. 2001;68(4):403–16. doi: 10.1016/S0013-7944(00)00103-X.

[4] Melenk JM, Babuška I. The partition of unity finite element method: Basic theory and applications. Comput Methods Appl Mech Eng. 1996;139(1–4):289–314. doi: 10.1016/S0045-7825(96)01087-0.

[5] Sukumar N, Chopp DL, Moran B. Extended finite element method and fast marching method for three-dimensional fatigue crack propagation. Eng Fract Mech. 2003;70(1):29–48. doi: 10.1016/S0013-7944(02)00032-2.

[6] Sukumar N, Chopp DL, Moes N, Belytschko T. Modeling holes and inclusions by level sets in the extended finite-element method. Comput Methods Appl Mech Eng. 2001;190(46–47):6183–200.

[7] Asadpoure A, Mohammadi S, Vafai A. Modeling crack in orthotropic media using a coupled finite element and partition of unity methods. Finite Elem Anal Des. 2006;42(13):1165–75. doi: 10.1016/j.finel.2006.05.001.

[8] Asadpoure A, Mohammadi S, Vafai A. Crack analysis in orthotropic media using the extended finite element method. Thin-Walled Struct. 2006;44(9):1031–8. doi: 10.1016/j.tws.2006.07.007.

[9] Motamedi D, Mohammadi S. Dynamic crack propagation analysis of orthotropic media by the extended finite element method. Int J Fract. 2010;161(1):21–39. doi: 10.1007/s10704-009-9423-7.

[10] Motamedi D, Mohammadi S. Dynamic analysis of fixed cracks in composites by the extended finite element method. Eng Fract Mech. 2010;77(17):3373–93. doi: 10.1016/j.engfracmech.2010.08.011.

[11] Esna Ashari S, Mohammadi S. Fracture analysis of FRP-reinforced beams by orthotropic XFEM. J Compos Mater. 2012;46(11):1367–89. doi: 10.1177/0021998311418702.

[12] Hughes TJR, Cottrell JA, Bazilevs Y. Isogeometric analysis: CAD, finite elements, NURBS, exact geometry and mesh refinement. Comput Methods Appl Mech Eng. 2005;194(39–41):4135–95. doi: 10.1016/j.cma.2004.10.008.

[13] Manh ND, Evgrafov A, Gersborg AR, Gravesen J. Isogeometric shape optimization of vibrating membranes. Comput Methods Appl Mech Eng. 2011;200(13–16):1343–53. doi: 10.1016/j.cma.2010.12.015.

[14] Qian X, Sigmund O. Isogeometric shape optimization of photonic crystals via Coons patches. Comput Methods Appl Mech Eng. 2011;200(25–28):2237–55. doi: 10.1016/j.cma.2011.03.007.

[15] Casanova CF, Gallego A. NURBS-based analysis of higher-order composite shells. Compos Struct. 2013;104:125–33. doi: 10.1016/j.compstruct.2013.04.024.

[16] Benson DJ, Bazilevs Y, Hsu MC, Hughes TJ. A large deformation, rotation-free, isogeometric shell. Comput Methods Appl Mech Eng. 2011;200(13–16):1367–78. doi: 10.1016/j.cma.2010.12.003.

[17] Valizadeh N, Natarajan S, Gonzalez-Estrada OA, Rabczuk T, Bui TQ, Bordas SPA. NURBS-based finite element analysis of functionally graded plates: Static bending, vibration, buckling and flutter. Compos Struct. 2013;99:309–26. doi: 10.1016/j.compstruct.2012.11.008.

[18] Thai CH, Ferreira AJM, Carrera E, Nguyen-Xuan H. Isogeometric analysis of laminated composite and sandwich plates using a layerwise deformation theory. Compos Struct. 2013;104:196–214. doi: 10.1016/j.compstruct.2013.04.002.

[19] Mohammadi S, Ghorashi SS, Valizadeh N. Extended isogeometric analysis for simulation of stationary and propagating cracks. Int J Numer Methods Eng. 2011;89:1069–101.

[20] De Luycker E, Benson DJ, Belytschko T, Bazilevs Y, Hsu MC. X-FEM in isogeometric analysis for linear fracture mechanics. Int J Numer Methods Eng. 2011;87(6):541–65.

[21] Yao XF, Xu W, Arakawa K, Takahashi K, Mada T. Dynamic optical visualization on the interaction between propagating crack and stationary crack. Opt Lasers Eng. 2005;43(2):195–207. doi: 10.1016/j.optlaseng.2004.06.003.

[22] Tabarraei A, Sukumar N. Extended finite element method on polygonal and quadtree meshes. Comput Methods Appl Mech Eng. 2008;197(5):425–38. doi: 10.1016/j.cma.2007.08.013.

[23] Bayesteh H, Afshar A, Mohammdi S. Thermo-mechanical fracture study of inhomogeneous cracked solids by the extended isogeometric analysis method. Eur J Mech A/Solids. 2015;51:123–39. doi: 10.1016/j.euromechsol.2014.12.004.

[24] Yadav A, Patil RU, Singh SK, Godara RK, Bhardwaj G. A thermo-mechanical fracture analysis of linear elastic materials using XIGA. Mech Adv Mater Struct. 2022;29(12):1730–55. doi: 10.1080/15376494.2020.1838006.

[25] Lal A, Vaghela MB, Mishra K. Numerical analysis of an edge crack isotropic plate with void/inclusions under different loading by implementing XFEM. J Appl Comput Mech. 2021;7(3):1362–82. doi: 10.22055/jacm.2019.31268.1848.

[26] Lal A, Mishra K. Stochastic MMSIF of multiple edge cracks FGMs plates subjected to combined loading using XFEM. Curved Layer Struct. 2020;7(1):35–47. doi: 10.1515/cls-2020-0004.

[27] Palekar SP, Lal A. Stochastic fracture analysis of the laminated composite plates subjected to different types of biaxially applied stresses by implementing SXFEM. Iran J Sci Technol - Trans Mech Eng. 2022;46(2):509–30. doi: 10.1007/s40997-021-00434-4.

[28] Chopra PS, Wang PY, Hartz BJ. Probabilistic prediction of multiple fracture under service conditions. Nucl Eng Des. 1974;28(3):446–58. doi: 10.1016/0029-5493(74)90213-1.

[29] Rahman S. Probabilistic fracture mechanics: J-estimation and finite element methods. Am Soc Mech Eng Press Vessel Pip Div PVP. 1998;373:9–18.

[30] Chen G, Rahman S, Park YH. Shape sensitivity and reliability analyses of linear-elastic cracked structures. Int J Fract. 2001;112(3):223–46. doi: 10.1023/A:1013543913779.

[31] Wu XF, Dzenis YA. Experimental determination of probabilistic edge-delamination strength of a graphite-fiber/epoxy composite. Compos Struct. 2005;70(1):100–8. doi: 10.1016/j.compstruct.2004.08.016.

[32] Alkhateb H, Al-Ostaz A, Alzebdeh KI. Developing a stochastic model to predict the strength and crack path of random composites. Compos Part B Eng. 2009;40(1):7–16. doi: 10.1016/j.compositesb.2008.09.001.

[33] Chowdhury MS, Song C, Gao W. Probabilistic fracture mechanics by using Monte Carlo simulation and the scaled boundary finite element method. Eng Fract Mech. 2011;78(12):2369–89. doi: 10.1016/j.engfracmech.2011.05.008.

[34] Rahman S, Chakraborty A. Stochastic multiscale fracture analysis of three-dimensional functionally graded composites. Eng Fract Mech. 2011;78(1):27–46. doi: 10.1016/j.engfracmech.2010.09.006.

[35] Sobey AJ, Blake JIR, Shenoi RA. Monte Carlo reliability analysis of tophat stiffened composite plate structures under out of plane loading. Reliab Eng Syst Saf. 2013;110:41–9. doi: 10.1016/j.ress.2012.08.011.

[36] Vu-Bac N, Rafiee R, Zhuang X, Lahmer T, Rabczuk T. Uncertainty quantification for multiscale modeling of polymer nanocomposites with correlated parameters. Compos Part B Eng. 2015;68:446–64. doi: 10.1016/j.compositesb.2014.09.008.

[37] Lal A, Mulani SB, Kapania RK. Stochastic critical stress intensity factor response of single edge notched laminated composite plate using displacement correlation method. Mech Adv Mater Struct. 2020;27(14):1223–37. doi: 10.1080/15376494.2018.1506067.

[38] Lal A, Palekar SP. Stochastic fracture analysis of laminated composite plate with arbitrary cracks using X-FEM. Int J Mech Mater Des. 2017;13(2):195–228. doi: 10.1007/s10999-015-9325-y.

[39] Hosseini SS, Bayesteh H, Mohammadi S. Thermo-mechanical XFEM crack propagation analysis of functionally graded materials. Mater Sci Eng A. 2013;561:285–302. doi: 10.1016/j.msea.2012.10.043.

[40] Bayesteh H, Mohammadi S. XFEM fracture analysis of orthotropic functionally graded materials. Compos Part B Eng. 2013;44(1):8–25. doi: 10.1016/j.compositesb.2012.07.055.

[41] Prasad NNV, Aliabadi MH, Rooke DP. The dual boundary element method for thermoelastic crack problems. Int J Fract. 1994;66(3):255–72. doi: 10.1007/BF00042588.

[42] Raveendra ST, Banerjee PK. Boundary element analysis of cracks in thermally stressed planar structures. Int J Solids Struct. 1992;29(18):2301–17. doi: 10.1016/0020-7683(92)90217-H.

[43] Shih CF, Moran B, Nakamura T. Energy release rate along a three-dimensional crack front in a thermally stressed body. Int J Fract. 1986;30(2):79–102. doi: 10.1007/BF00034019.

[44] Wilson WK, Yu IW. The use of the J-integral in thermal stress crack problems. Int J Fract. 1979;15(4):377–87. doi: 10.1007/BF00033062.

[45] Dimitri R, De Lorenzis L, Wriggers P, Zavarise G. NURBS- and T-spline-based isogeometric cohesive zone modeling of interface debonding. Comput Mech. 2014;54:369–88. doi: 10.1007/s00466-014-0991-7.

[46] Dimitri R, Fantuzzi N, Tornabene F, Zavarise G. Innovative numerical methods based on SFEM and IGA for computing stress concentrations in isotropic plates with discontinuities. Int J Mech Sci. 2016;118:166–87. doi: 10.1016/j.ijmecsci.2016.09.020.

[47] Dimitri R, Fantuzzi N, Li Y, Tornabene F. Numerical computation of the crack development and SIF in composite materials with Xfem and Sfem. Compos Struct. 2016;160:468–90. doi: 10.1016/j.compstruct.2016.10.067.

[48] Dimitri R, Rinaldi M, Trullo M. Theoretical and computational investigation of the fracturing behavior of anisotropic geomaterials. Contin Mech Thermodyn. 2023;35(4):1417–32. doi: 10.1007/s00161-022-01141-4.

[49] Asadpoure A, Mohammadi S. Developing new enrichment functions for crack simulation in orthotropic media by the extended finite element method. Int J Numer Methods Eng. 2007;69:2150–72.

[50] Sih GRI, Co G, Paris PC. On cracks in rectiltnearly anisotropic bodies. Int J Fract. 1965;1:189–203.

[51] Haldar SMA. Book review. Nippon Genshiryoku Gakkaishi/J Energy Soc Jpn. 2001;43(7):675.

[52] Akramin MRM, Alshoaibi A, Hadi MSA, Ariffin AK, Mohamed NAN. Probabilistic analysis of linear elastic cracked structures. J Zhejiang Univ Sci A. 2007;8(11):1795–9. doi: 10.1631/jzus.2007.A1795.